

# Oxidative Dehydrogenation of Propane over $V_2O_5/MoO_3/Al_2O_3$ and $V_2O_5/Cr_2O_3/Al_2O_3$ : Structural Characterization and Catalytic Function

Shuwu Yang, Enrique Iglesia,\* and Alexis T. Bell\*

Chemical Sciences Division, Lawrence Berkeley National Laboratory, and Department of Chemical Engineering, University of California, Berkeley, California 94720-1462

Received: November 8, 2004; In Final Form: February 11, 2005

The structure and catalytic properties of binary dispersed oxide structures prepared by sequential deposition of  $VO_x$  and  $MoO_x$  or  $VO_x$  and  $CrO_x$  on  $Al_2O_3$  were examined using Raman and UV–visible spectroscopies, the dynamics of stoichiometric reduction in  $H_2$ , and the oxidative dehydrogenation of propane.  $VO_x$  domains on  $Al_2O_3$  modified by an equivalent  $MoO_x$  monolayer led to dispersed binary structures at all surface densities.  $MoO_x$  layers led to higher reactivity for  $VO_x$  domains present at low  $VO_x$  surface densities by replacing V–O–Al structures with more reactive V–O–Mo species. At higher surface densities, V–O–V structures in prevalent polyvanadates were replaced with less reactive V–O–Mo, leading to lower reducibility and oxidative dehydrogenation rates. Raman, reduction, and UV–visible data indicate that polyvanadates predominant on  $Al_2O_3$  convert to dispersed binary oxide structures when  $MoO_x$  is deposited before or after  $VO_x$  deposition; these structures are less reducible and show higher UV–visible absorption energies than polyvanadate structures on  $Al_2O_3$ . The deposition sequence in binary Mo–V catalysts did not lead to significant differences in structure or catalytic rates, suggesting that the two active oxide components become intimately mixed. The deposition of  $CrO_x$  on  $Al_2O_3$  led to more reactive  $VO_x$  domains than those deposited on pure  $Al_2O_3$  at similar  $VO_x$  surface densities. At all surface densities, the replacement of V–O–Al or V–O–V structures with V–O–Cr increased the reducibility and catalytic reactivity of  $VO_x$  domains; it also led to higher propene selectivities via the selective inhibition of secondary  $C_3H_6$  combustion pathways, prevalent in  $VO_x-Al_2O_3$ , and of  $C_3H_8$  combustion routes that lead to low alkene selectivities on  $CrO_x-Al_2O_3$ .  $VO_x$  and  $CrO_x$  mix significantly during synthesis or thermal treatment to form  $CrVO_4$  domains. The deposition sequence, however, influences catalytic selectivities and reduction rates, suggesting the retention of some of the component deposited last as unmixed domains exposed at catalyst surfaces. These findings suggest that the reduction and catalytic properties of active  $VO_x$  domains can be modified significantly by the formation of binary dispersed structures.  $VO_x-CrO_x$  structures, in particular, lead to higher oxidative dehydrogenation rates and selectivities than do  $VO_x$  domains present at similar surface densities on pure  $Al_2O_3$  supports.

## 1. Introduction

The oxidative dehydrogenation (ODH) of propane provides an attractive route for the synthesis of propene.<sup>1–15</sup> This reaction occurs on oxides of V,<sup>16–31</sup> Mo,<sup>19,23,38–44</sup> and Cr,<sup>39–46</sup> with V-based catalysts typically providing higher rates and propene selectivities.<sup>19,23</sup> Supports influence rates and selectivities on dispersed  $VO_x$  domains.<sup>17,20</sup> For example,  $VO_x$  supported on  $ZrO_2$ <sup>16,30,31</sup> is highly active but gives low propene selectivities, while  $VO_x/Al_2O_3$  gives lower rates but much higher alkene selectivities.<sup>17,20</sup>

ODH reactions on supported  $VO_x$  catalysts involve redox cycles and kinetically relevant C–H bond activation steps that require electron transfer from O to V within  $VO_x$  domains.<sup>18,19,23,35,47</sup> Chen et al.<sup>23</sup> showed that ODH turnover rates increase with decreasing  $VO_x$  UV–visible absorption edge energies and with increasing reducibility of  $VO_x$  domains in  $H_2$ . ODH turnover rates increased as polyvanadates became the predominant  $VO_x$  species, suggesting that linkages between monovanadate structures and support cations decrease the reactivity and reducibility of V–oxo species. These data also

suggested that an intervening layer of a more reducible oxide ( $MO_x$ ) may minimize these support effects by replacing V–O–support linkages with more reactive V–O–M linkages.

Few such binary dispersed oxide catalysts have been reported. Gao et al.<sup>48</sup> and Liu et al.<sup>49</sup> reported the catalytic properties of  $V_2O_5/TiO_2/SiO_2$  for  $CH_3OH$  oxidation and  $VO_x/SnO_x/Al_2O_3$  for  $CH_3OCH_3$  oxidation, respectively. In both studies, the intervening layer increased the reducibility and catalytic activity of  $VO_x$  domains. Such binary dispersed structures have also been examined for ODH reactions. Cherian et al.<sup>40</sup> reported that  $VO_x$  structures on  $Al_2O_3$  and  $TiO_2$  supported modified by  $CrO_x$  gave higher rates but lower propene selectivities than catalysts containing only  $VO_x$  domains on these supports. The latter study reported a single composition, without systematic examination of any structural implications and catalytic consequences of compositional changes. Dai et al.<sup>50</sup> described a series of binary dispersed  $VO_x/MoO_x/Al_2O_3$  catalysts prepared by dispersing  $VO_x$  on  $Al_2O_3$  modified by a nominal polymolybdate monolayer. For a given  $VO_x$  surface density, active structures on  $MoO_x$ -coated  $Al_2O_3$  were more reducible than those on  $Al_2O_3$ , apparently because less reactive V–O–Al linkages are replaced with V–O–Mo bonds; these trends were also reflected in the higher propane ODH turnover rates measured on  $VO_x$  structures

\* Corresponding authors. E-mail: bell@cchem.berkeley.edu (A.T.B.); iglesias@cchem.berkeley.edu (E.I.).

dispersed in  $\text{MoO}_x/\text{Al}_2\text{O}_3$  relative to those on similar  $\text{VO}_x$  domains on pure  $\text{Al}_2\text{O}_3$  supports.  $\text{MoO}_x$  interlayers also decreased primary and secondary combustion rates and led to higher propene selectivities. In contrast, Bañares and Khatib<sup>51</sup> found no synergistic effects in  $\text{VO}_x\text{-MoO}_x/\text{Al}_2\text{O}_3$  samples prepared by coimpregnation, which contained Mo–V–O mixed phases at (Mo + V) surface densities above those required for two-dimensional oxo-oligomers on  $\text{Al}_2\text{O}_3$  surfaces.

Here, we aim to probe the structure and catalytic function of binary dispersed oxide catalysts for alkane ODH reactions. Samples were prepared by dispersing  $\text{VO}_x$  species on  $\text{Al}_2\text{O}_3$  support surfaces modified by Mo and Cr oxides and also by preparing “inverse bilayers”, in which Mo and Cr oxides are dispersed on  $\text{Al}_2\text{O}_3$  modified by a polyvanadate monolayer. The resulting structures were examined by Raman and UV–visible spectroscopies and by measurements of their reduction dynamics in  $\text{H}_2$ , and their catalytic function was determined by rigorous measurements of turnover rates and of rate constants for primary and secondary reactions.

## 2. Experimental Section

### 2.1. Synthesis of Binary Dispersed Structures on $\text{Al}_2\text{O}_3$ .

Fumed  $\text{Al}_2\text{O}_3$  (Degussa AG; surface area 107  $\text{m}^2/\text{g}$ ) was contacted with deionized water, dried at 383 K for 72 h, and treated in ambient air at 823 K for 3 h before use in a process intended to strengthen aggregates; its BET surface area was 125  $\text{m}^2/\text{g}$  after this treatment.  $\text{MoO}_x/\text{Al}_2\text{O}_3$  (MoAl) and  $\text{CrO}_x/\text{Al}_2\text{O}_3$  (CrAl) with various active oxide surface densities were prepared by impregnating  $\text{Al}_2\text{O}_3$  with solutions of molybdenyl acetylacetonate (Alfa Aesar, 99%) in acetone (Aldrich, 99.5%) or with aqueous solutions of chromium(III) nitrate nonahydrate (Aldrich, 98%). Samples were then dried at 383 K in ambient air overnight and treated in flowing dry air (Airgas, zero grade, 3.33  $\text{cm}^3 \text{ s}^{-1}$ ) by heating to 773 K at 0.167  $\text{K s}^{-1}$  and then holding at 773 K for 2 h.  $\text{VO}_x/\text{Al}_2\text{O}_3$  (VAl) was prepared by incipient-wetness impregnation of  $\text{Al}_2\text{O}_3$  with 2-propanol (Aldrich, 99.99%) solutions of vanadyl isopropoxide (Aldrich, 98%); samples were kept in a  $\text{N}_2$  flow within a glovebox overnight and transferred into a quartz reactor sealed with stopcocks at each end. These samples were treated at 393 K in flowing  $\text{N}_2$  (Airgas, 99.999%, 1.67  $\text{cm}^3 \text{ s}^{-1}$ ) for 1 h and at 573 K for 1 h; air (Airgas, zero grade, 1.67  $\text{cm}^3 \text{ s}^{-1}$ ) was then introduced and samples were held at 573 K for 1 h and at 773 K for 2 h.

Binary dispersed  $\text{VO}_x/\text{MoO}_x/\text{Al}_2\text{O}_3$  (VMoAl) and  $\text{VO}_x/\text{CrO}_x/\text{Al}_2\text{O}_3$  (VCrAl) catalysts were prepared by incipient-wetness impregnation of MoAl or CrAl samples with 2-propanol solutions of vanadyl isopropoxide with the same procedures used for VAl.  $\text{MoO}_x/\text{VO}_x/\text{Al}_2\text{O}_3$  (MoVAl) catalysts with varying  $\text{MoO}_3$  contents were prepared by impregnation of 10%  $\text{V}_2\text{O}_5/\text{Al}_2\text{O}_3$  with acetone solutions of molybdenyl acetylacetonate, and then treating them at 383 K in ambient air and in flowing dry air at 773 K for 2 h. A 12%  $\text{Cr}_2\text{O}_3/10\% \text{V}_2\text{O}_5/\text{Al}_2\text{O}_3$  (12Cr10VAl) sample was prepared by incipient-wetness impregnation of 10%  $\text{V}_2\text{O}_5/\text{Al}_2\text{O}_3$  with aqueous chromium(III) nitrate solutions, followed by drying at 383 K in ambient air and treatment in flowing dry air at 773 K for 2 h.

**2.2. Catalyst Characterization.** BET surface areas were measured using Quantasorb units (Quantasorb 1 or Quantasorb 6 Surface Analyzers, Quantachrome Corp.) and  $\text{N}_2$  at its normal boiling point. Samples were treated in dynamic vacuum (0.1 Pa) at 393 K for at least 3 h before BET measurements. X-ray diffraction (XRD) data were measured with a Siemens D5000 unit at ambient temperature using  $\text{Cu K}\alpha$  radiation. The X-ray tube was operated at 45 kV and 35 mA, and the scan rate was 1.2°/min.

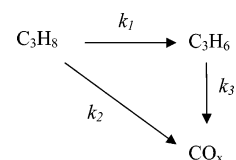
Raman spectra were collected using a Hololab Series 5000 spectrometer (Kaiser Optical) equipped with a frequency-doubled 75-mW Nd:YAG laser (532 nm). Samples were pressed into self-supported wafers (0.9 cm diameter,  $\sim 50 \text{ mg cm}^{-2}$ ) at 200 MPa and then held onto a rotating holder within a quartz Raman cell. Raman spectra were recorded at ambient temperature before and after treating samples in flowing dry air (Airgas, zero grade, 0.83  $\text{cm}^3 \text{ s}^{-1}$ ) while heating to 673 K at 0.167  $\text{K s}^{-1}$  and holding at 673 K for 1 h.

Temperature-programmed reduction (TPR) studies were carried out in a flow unit (QS-10, Quantachrome Corp.).  $\text{H}_2$  concentrations were measured using a thermal conductivity detector calibrated by reducing  $\text{CuO}$ . The sample amount (15–100 mg) was chosen to maintain a constant number of removable oxygen atoms (equivalent to 5 mg of  $\text{MoO}_3$ ). Samples were heated to 1173 K in 20%  $\text{H}_2\text{-Ar}$  (Praxair, 99.999%) at 0.167  $\text{K s}^{-1}$  and held at 1173 K for 1 h.  $\text{H}_2\text{O}$  reduction products were removed before thermal conductivity detection with a 13X sieve at ambient temperature.

Diffuse reflectance UV–visible spectra were collected with a Cary 4 spectrophotometer (Varian Corp.) equipped with a Harrick Scientific diffuse reflectance attachment (DRP-XXX) and an environmental chamber (DRA-2CR). Samples were treated in 20%  $\text{O}_2\text{-He}$  (Praxair, 99.999%, 0.83  $\text{cm}^3 \text{ s}^{-1}$ ) at 723 K for 0.5 h before measurements. The Kubelka–Munk function ( $F(R_\infty)$ ) was used to convert reflectance data into pseudoabsorbance using  $\text{MgO}$  as a reflective standard.<sup>52,53</sup> Absorption-edge energies were calculated from the  $x$ -intercept of a linear regression of  $[(F(R_\infty))/h\nu]^{1/2}$  data versus  $h\nu$ .<sup>53</sup>

**2.3. Catalytic Rates and Selectivity Measurements.** Oxidative dehydrogenation rates and selectivities were measured at 583–673 K using a quartz flow microreactor. The reactor is 50 cm long, and the catalyst section is 10 mm in diameter and 35 mm in length. The reactor was heated via an electrical furnace, and the temperature was set by a temperature controller (WATLOW) and measured by a K-type thermocouple inserted into the reactor and positioned within the catalyst bed. Temperature gradients were avoided by diluting catalyst samples (20–40 mg, 250–500  $\mu\text{m}$ ) with equal amounts of acid-washed quartz (250–500  $\mu\text{m}$ ).  $\text{C}_3\text{H}_8$  (13.5 kPa, Airgas, 99.9%) and  $\text{O}_2$  (1.7 kPa, Airgas, 99.999%) with He as balance (Airgas, 99.999%) were used as reactants.  $\text{C}_3\text{H}_8$  and  $\text{O}_2$  conversions were kept below 2% and 20%, respectively, by varying reactant flow rates. Space velocities were 30 000–500 000  $\text{cm}^3 \text{ g}^{-1} \text{ h}^{-1}$ . Reactant and product concentrations were measured by chromatography (Hewlett-Packard 6890) using a Carboxen 1004 packed column connected to a thermal conductivity detector and HP-PLOT Q capillary column with a flame ionization detector.

Reactor residence time effects on rates and selectivities were used to estimate  $\text{C}_3\text{H}_8$  dehydrogenation ( $r_1$ ) and combustion ( $r_2$ ) rates by extrapolating  $\text{C}_3\text{H}_6$  and  $\text{CO}_x$  synthesis rates to zero residence time.  $\text{C}_3\text{H}_6$  combustion rates ( $r_3$ ) were obtained from the slope of  $\text{C}_3\text{H}_6$  selectivity data as a function of residence time.<sup>16–23</sup> These primary and secondary reactions and their respective rate constants ( $k_1$ ,  $k_2$ ,  $k_3$ ) are shown in the scheme below:



Dehydrogenation and combustion rates are assumed to be first-order in  $\text{C}_3\text{H}_8$  and  $\text{C}_3\text{H}_6$  and zero-order in  $\text{O}_2$ , as found

**TABLE 1: BET Surface Areas and VO<sub>x</sub> Surface Density of V<sub>2</sub>O<sub>5</sub>/Al<sub>2</sub>O<sub>3</sub> Catalysts**

catalyst	denotation	wt % V <sub>2</sub> O <sub>5</sub> <sup>a</sup>	surface area (m <sup>2</sup> /g cat)	surface area (m <sup>2</sup> /g Al <sub>2</sub> O <sub>3</sub> )	VO <sub>x</sub> surface density (V/nm <sup>2</sup> )
3% V <sub>2</sub> O <sub>5</sub> /Al <sub>2</sub> O <sub>3</sub>	3VAI	3.1	108.1	111.6	1.9
7% V <sub>2</sub> O <sub>5</sub> /Al <sub>2</sub> O <sub>3</sub>	7VAI	7.3	119.3	128.7	4.1
10% V <sub>2</sub> O <sub>5</sub> /Al <sub>2</sub> O <sub>3</sub>	10VAI	8.3	103.3	112.6	5.3
15% V <sub>2</sub> O <sub>5</sub> /Al <sub>2</sub> O <sub>3</sub>	15VAI	12.4	94.8	108.3	8.7
18% V <sub>2</sub> O <sub>5</sub> /Al <sub>2</sub> O <sub>3</sub>	18VAI	14.8	91.1	106.9	10.7

<sup>a</sup> Weight loading obtained by inductively coupled plasma (ICP) analysis.

**TABLE 2: BET Surface Areas and VO<sub>x</sub> Surface Density of V<sub>2</sub>O<sub>5</sub>/MoO<sub>3</sub>/Al<sub>2</sub>O<sub>3</sub> and MoO<sub>3</sub>/V<sub>2</sub>O<sub>5</sub>/Al<sub>2</sub>O<sub>3</sub> Catalysts**

catalyst	denotation	wt % V <sub>2</sub> O <sub>5</sub>	surface area (m <sup>2</sup> /g cat)	surface area (m <sup>2</sup> /g Al <sub>2</sub> O <sub>3</sub> )	VO <sub>x</sub> surface density (V/nm <sup>2</sup> )
12% MoO <sub>3</sub> /Al <sub>2</sub> O <sub>3</sub>	12MoAl		99.4	113.0	5.0 (Mo/nm <sup>2</sup> )
3% V <sub>2</sub> O <sub>5</sub> /12% MoO <sub>3</sub> /Al <sub>2</sub> O <sub>3</sub>	3V12MoAl	2.2 <sup>a</sup>	90.1	104.7	1.6
7% V <sub>2</sub> O <sub>5</sub> /12% MoO <sub>3</sub> /Al <sub>2</sub> O <sub>3</sub>	7V12MoAl	6.1 <sup>a</sup>	90.8	109.8	4.4
10% V <sub>2</sub> O <sub>5</sub> /12% MoO <sub>3</sub> /Al <sub>2</sub> O <sub>3</sub>	10V12MoAl	8.4 <sup>a</sup>	81.2	100.7	6.9
15% V <sub>2</sub> O <sub>5</sub> /12% MoO <sub>3</sub> /Al <sub>2</sub> O <sub>3</sub>	15V12MoAl	12.4 <sup>a</sup>	84.6	109.8	9.7
10% V <sub>2</sub> O <sub>5</sub> /2% MoO <sub>3</sub> /Al <sub>2</sub> O <sub>3</sub>	10V2MoAl	8.4 <sup>b</sup>	105.5	117.4	5.3
10% V <sub>2</sub> O <sub>5</sub> /4% MoO <sub>3</sub> /Al <sub>2</sub> O <sub>3</sub>	10V4MoAl	8.4 <sup>b</sup>	89.9	102.2	6.2
10% V <sub>2</sub> O <sub>5</sub> /8% MoO <sub>3</sub> /Al <sub>2</sub> O <sub>3</sub>	10V8MoAl	8.4 <sup>b</sup>	83.8	99.4	6.6
10% V <sub>2</sub> O <sub>5</sub> /16% MoO <sub>3</sub> /Al <sub>2</sub> O <sub>3</sub>	10V16MoAl	8.4 <sup>b</sup>	77.3	100.4	7.2
10% V <sub>2</sub> O <sub>5</sub> /20% MoO <sub>3</sub> /Al <sub>2</sub> O <sub>3</sub>	10V20MoAl	8.4 <sup>b</sup>	74.5	101.6	7.5

<sup>a</sup> Weight loading obtained by inductively coupled plasma (ICP) analysis. <sup>b</sup> Assuming that 10VxMoAl has the same V<sub>2</sub>O<sub>5</sub> loading as 10V12MoAl.

**TABLE 3: BET Surface Areas and VO<sub>x</sub> Surface Density of V<sub>2</sub>O<sub>5</sub>/Cr<sub>2</sub>O<sub>3</sub>/Al<sub>2</sub>O<sub>3</sub> Catalysts**

catalyst	denotation	wt % V <sub>2</sub> O <sub>5</sub>	surface area (m <sup>2</sup> /g cat)	surface area (m <sup>2</sup> /g Al <sub>2</sub> O <sub>3</sub> )	VO <sub>x</sub> surface density (V/nm <sup>2</sup> )
12% Cr <sub>2</sub> O <sub>3</sub> /Al <sub>2</sub> O <sub>3</sub>	12CrAl		120.0	136.4	7.9 (Cr/nm <sup>2</sup> )
1% V <sub>2</sub> O <sub>5</sub> /12% Cr <sub>2</sub> O <sub>3</sub> /Al <sub>2</sub> O <sub>3</sub>	1V12CrAl	1.0 <sup>a</sup>	112.6	129.2	0.6
3% V <sub>2</sub> O <sub>5</sub> /12% Cr <sub>2</sub> O <sub>3</sub> /Al <sub>2</sub> O <sub>3</sub>	3V12CrAl	3.0 <sup>a</sup>	94.8	111.1	2.1
7% V <sub>2</sub> O <sub>5</sub> /12% Cr <sub>2</sub> O <sub>3</sub> /Al <sub>2</sub> O <sub>3</sub>	7V12CrAl	6.4 <sup>a</sup>	98.6	119.7	4.3
10% V <sub>2</sub> O <sub>5</sub> /12% Cr <sub>2</sub> O <sub>3</sub> /Al <sub>2</sub> O <sub>3</sub>	10V12CrAl	8.9 <sup>a</sup>	93.0	116.0	6.3
12% V <sub>2</sub> O <sub>5</sub> /12% Cr <sub>2</sub> O <sub>3</sub> /Al <sub>2</sub> O <sub>3</sub>	12V12CrAl	10.4 <sup>a</sup>	91.6	116.2	7.5
15% V <sub>2</sub> O <sub>5</sub> /12% Cr <sub>2</sub> O <sub>3</sub> /Al <sub>2</sub> O <sub>3</sub>	15V12CrAl	12.8 <sup>a</sup>	90.5	117.9	9.4
10% V <sub>2</sub> O <sub>5</sub> /1% Cr <sub>2</sub> O <sub>3</sub> /Al <sub>2</sub> O <sub>3</sub>	10V1CrAl	8.9 <sup>b</sup>	106.3	117.8	5.5
10% V <sub>2</sub> O <sub>5</sub> /3% Cr <sub>2</sub> O <sub>3</sub> /Al <sub>2</sub> O <sub>3</sub>	10V3CrAl	8.9 <sup>b</sup>	105.5	119.3	5.6
10% V <sub>2</sub> O <sub>5</sub> /6% Cr <sub>2</sub> O <sub>3</sub> /Al <sub>2</sub> O <sub>3</sub>	10V6CrAl	8.9 <sup>b</sup>	91.7	107.1	6.4
10% V <sub>2</sub> O <sub>5</sub> /9% Cr <sub>2</sub> O <sub>3</sub> /Al <sub>2</sub> O <sub>3</sub>	10V9CrAl	8.9 <sup>b</sup>	96.5	116.4	6.1
10% V <sub>2</sub> O <sub>5</sub> /15% Cr <sub>2</sub> O <sub>3</sub> /Al <sub>2</sub> O <sub>3</sub>	10V15CrAl	8.9 <sup>b</sup>	90.5	116.8	6.5

<sup>a</sup> Weight loading obtained by inductively coupled plasma (ICP) analysis. <sup>b</sup> Assuming that 10VxCrAl has the same V<sub>2</sub>O<sub>5</sub> loading as 10V12CrAl.

experimentally on MoO<sub>x</sub> and VO<sub>x</sub> catalysts.<sup>16–21</sup> Values of  $k_2/k_1$  are calculated from primary selectivities ( $S_{C_3H_6}^0$ ) using

$$S_{C_3H_6}^0 = k_1/(k_1 + k_2)$$

while  $k_3$  is obtained from C<sub>3</sub>H<sub>6</sub> selectivities using

$$S_{C_3H_6} = S_{C_3H_6}^0 [1 - (k_1 + k_2 + k_3)C_v\tau/2]$$

where  $\tau$  is the residence time and  $C_v$  is the number of V-atoms per unit volume.<sup>17</sup>

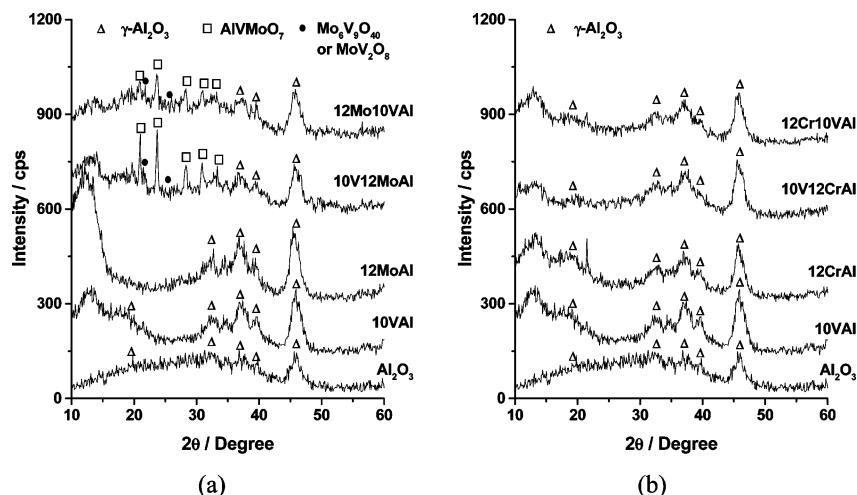
### 3. Results and Discussion

**3.1. Catalyst Characterization.** *3.1.1. Surface Areas and Structure of Catalysts.* Surface areas and VO<sub>x</sub> surface densities for all samples, as well as their designated nomenclature, are shown in Tables 1–3. Surface areas of VAl samples decreased with increasing VO<sub>x</sub> content and surface density (Table 1), as was also found for VO<sub>x</sub> dispersed on Al<sub>2</sub>O<sub>3</sub> containing a nominal monolayer of MoO<sub>x</sub> (12MoAl) or CrO<sub>x</sub> (12CrAl). Surface areas for VMoAl and VCrAl with similar VO<sub>x</sub> surface densities but varying MoO<sub>x</sub> or CrO<sub>x</sub> contents also decreased with increasing MoO<sub>x</sub> and CrO<sub>x</sub> content (Tables 2 and 3). These changes in

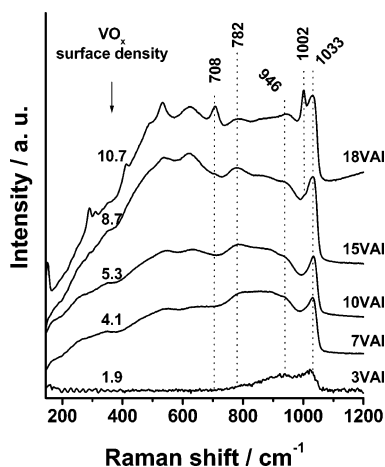
surface areas merely reflect the larger total mass of samples per amount of Al<sub>2</sub>O<sub>3</sub> in each sample; surface areas per amount of Al<sub>2</sub>O<sub>3</sub> (Tables 1–3) are essentially the same in all samples. Thus, dispersing active oxides, as monolayers or bilayers, does not influence Al<sub>2</sub>O<sub>3</sub> surface area.

Figure 1 shows X-ray diffraction data for selected samples. Pure Al<sub>2</sub>O<sub>3</sub> shows only lines for its  $\gamma$ -phase, which is the only phase detected in 10VAI, 12MoAl, and 12CrAl. 10V12MoAl and 12Mo10VAI showed lines for AlVMoO<sub>7</sub> and weaker lines for Mo<sub>6</sub>V<sub>9</sub>O<sub>40</sub> and MoV<sub>2</sub>O<sub>8</sub>. Only  $\gamma$ -Al<sub>2</sub>O<sub>3</sub> was detected in 10V12CrAl and 12Cr10VAI.

Figure 2 shows Raman spectra at ambient temperature for VAl samples with a range of VO<sub>x</sub> surface densities treated in flowing dry air at 673 K for 1 h, and denoted as dehydrated samples throughout. The band at 1033 cm<sup>-1</sup> was assigned to V=O stretches in monovanadates and polyvanadates, and the broad 750–1000 cm<sup>-1</sup> bands were assigned to V–O–V stretches in two-dimensional polyvanadates.<sup>20,22,54–56</sup> Crystalline V<sub>2</sub>O<sub>5</sub> gives sharp intense Raman bands at 1002, 708, 535, 490, 410, 305, 289, 203, and 150 cm<sup>-1</sup>.<sup>2</sup> At low VO<sub>x</sub> surface densities (1.9 V/nm<sup>2</sup>), the ratio of the 1033 cm<sup>-1</sup> band intensity (V=O stretch) to that for the 946 cm<sup>-1</sup> band (V–O–V stretch) is high, indicating that monovanadates predominate on these samples.



**Figure 1.** XRD patterns of (a) Al<sub>2</sub>O<sub>3</sub>, 10VAI, 12MoAl, 10V12MoAl, and 12Mo10VAI and (b) Al<sub>2</sub>O<sub>3</sub>, 10VAI, 12CrAl, 10V12CrAl, and 12Cr10VAI. Assignments of diffraction peaks are based on the following PDF numbers:  $\gamma$ -alumina (PDF#10-0425), AlVMoO<sub>7</sub> (PDF#46-0687), Mo<sub>6</sub>V<sub>9</sub>O<sub>40</sub> (PDF#34-0527), and MoV<sub>2</sub>O<sub>8</sub> (PDF#74-0050).



**Figure 2.** Raman spectra of  $x$ VAI ( $x = 3-18$ ). Samples were treated in flowing dry air at 673 K for 1 h.

Polyvanadates become evident from emerging bands at 700–1000  $\text{cm}^{-1}$  as VO<sub>*x*</sub> surface density increases from 1.9 to 8.7  $\text{V}/\text{nm}^2$ . Crystalline V<sub>2</sub>O<sub>5</sub> was detected at high VO<sub>*x*</sub> surface density ( $>8 \text{ V}/\text{nm}^2$ ) from its two bands at 1002 and 708  $\text{cm}^{-1}$ , consistent with saturation of polyvanadate monolayers at 7–8  $\text{V}/\text{nm}^2$ .<sup>57</sup> Raman scattering cross sections for bulk V<sub>2</sub>O<sub>5</sub> are  $\sim 10$  times larger than for monovanadates.<sup>58</sup> Thus, dispersed VO<sub>*x*</sub> species remain predominant in 15VAI and 18VAI samples.

Raman spectra for dehydrated 12MoAl and V-coated 12MoAl samples with various VO<sub>*x*</sub> surface densities ( $x$ V12MoAl,  $x = 3-15$ ; 1.6–9.7  $\text{V}/\text{nm}^2$ ) are shown in Figure 3. 12MoAl showed bands at 1013 and 842  $\text{cm}^{-1}$ , attributed to Mo=O and Mo–O–Mo stretches, respectively.<sup>36,59–61</sup> Raman bands for crystalline MoO<sub>3</sub> were not detected on samples prepared using molybdenyl acetylacetonate as the precursor and a surface density of 5.0  $\text{Mo}/\text{nm}^2$ , corresponding to approximately one monolayer.<sup>62</sup> In contrast, MoAl samples prepared with ammonium heptamolybdate showed crystalline MoO<sub>3</sub> bands at surface densities above 4.5  $\text{Mo}/\text{nm}^2$ .<sup>36,50</sup> Only a small unresolved band at 1034  $\text{cm}^{-1}$ , assigned to V=O stretches, appeared when VO<sub>*x*</sub> was deposited on 12MoAl at low surface densities (Figure 3, 3V12MoAl; 1.6  $\text{V}/\text{nm}^2$ ). Higher VO<sub>*x*</sub> surface densities led to two new bands at 771 and 239  $\text{cm}^{-1}$ , together with a more intense band at 1013  $\text{cm}^{-1}$ , which was also present in the spectrum for 12MoAl. The 771  $\text{cm}^{-1}$  band was previously assigned to Mo–O–V stretches in molybdovanadates.<sup>50,51</sup> The

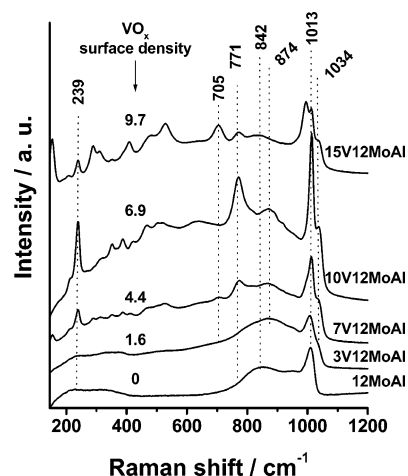


**Figure 3.** Raman spectra of 12MoAl and  $x$ V12MoAl ( $x = 3-15$ ) treated in flowing dry air at 673 K for 1 h.

intensities for the bands at 1013, 771, and 239  $\text{cm}^{-1}$  change to similar extents with increasing VO<sub>*x*</sub> surface density; thus, they appear to arise from a common V–Mo oxo-structure containing V–O–Mo linkages. A definitive assignment is not possible, but their sharp nature and concurrent appearance with AlMoVO<sub>7</sub> diffraction lines in 10V12MoAl (Figure 1) suggest that they arise from this crystalline phase. The 10V12MoAl sample, which contains an equivalent VO<sub>*x*</sub> monolayer on Al<sub>2</sub>O<sub>3</sub> pre-coated with a similar equivalent MoO<sub>*x*</sub> monolayer, showed the most intense bands at 1013, 771, and 239  $\text{cm}^{-1}$  (Figure 3), consistent with intimate mixing between VO<sub>*x*</sub> and MoO<sub>*x*</sub> species. Raman bands at 705 and 1002  $\text{cm}^{-1}$  for crystalline V<sub>2</sub>O<sub>5</sub> were detected at VO<sub>*x*</sub> surface densities of 9.7  $\text{V}/\text{nm}^2$  (15V12MoAl).

Raman spectra for 10V<sub>*x*</sub>MoAl ( $x = 4-20$ ) samples, which contain an equivalent VO<sub>*x*</sub> monolayer on Al<sub>2</sub>O<sub>3</sub> supports modified by varying amounts of MoO<sub>*x*</sub>, are shown in Figure 4. Raman spectra for 10V4MoAl (Figure 4) and 10VAI (Figure 2) are similar. Bands at 1013, 771, and 239  $\text{cm}^{-1}$ , corresponding to V–Mo–(Al)–O phases, were detected as MoO<sub>*x*</sub> surface density increased; these bands reached maximum intensities for 10V12MoAl, which contains equivalent monolayers of both VO<sub>*x*</sub> and MoO<sub>*x*</sub> components. Diffraction patterns suggest here also that these new bands arise from crystalline AlVMoO<sub>7</sub> structures. Crystalline MoO<sub>3</sub> was detected at surface densities above 6.9  $\text{Mo}/\text{nm}^2$ . The 1043  $\text{cm}^{-1}$  band for V=O stretching modes in monovanadates and polyvanadates decreased monotonically with

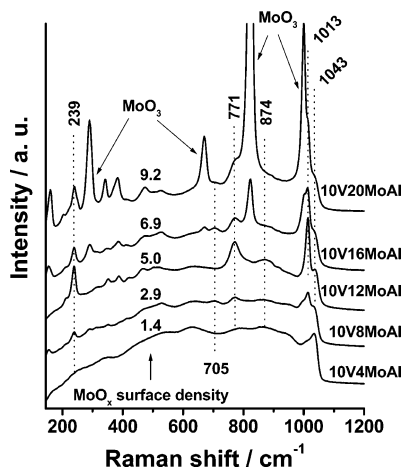


**Figure 4.** Raman spectra of  $10V_x\text{MoAl}$  ( $x = 4-20$ ) catalysts treated in flowing dry air at 673 K for 1 h.

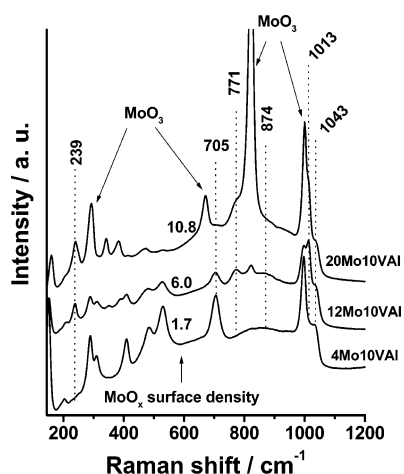


**Figure 5.** Raman spectra of  $x\text{Mo}10\text{VAl}$  ( $x = 4-20$ ) samples treated in flowing dry air at 673 K for 1 h.

increasing  $\text{MoO}_x$  surface density. Traces of crystalline  $\text{V}_2\text{O}_5$  were detected on  $10\text{V}8\text{MoAl}$  and  $10\text{V}16\text{MoAl}$ . The residual coexistence of crystalline  $\text{V}_2\text{O}_5$  and  $\text{MoO}_3$  in  $10\text{V}16\text{MoAl}$  indicates that  $\text{V}-\text{Mo}-\text{O}$  phases form more readily from dispersed  $\text{MoO}_x$  and  $\text{VO}_x$  than from crystalline  $\text{V}_2\text{O}_5$  and  $\text{MoO}_3$  at this treatment temperature.

$\text{MoO}_x$  species were supported on  $\text{Al}_2\text{O}_3$  precoated with an equivalent  $\text{VO}_x$  monolayer in an effort to explore the effects of deposition sequence on the structure and function of dispersed binary oxides. Figure 5 shows that a mixed  $\text{V}-\text{Mo}-\text{O}$  phase is present in  $12\text{Mo}10\text{VAl}$  and  $20\text{Mo}10\text{VAl}$  (bands at 1013, 771, and  $239\text{ cm}^{-1}$ ), but its characteristic bands are less intense than for similar compositions prepared via the reverse sequence (Figure 4;  $10\text{V}12\text{MoAl}$ ). Crystalline  $\text{V}_2\text{O}_5$  was detected in  $4\text{Mo}10\text{VAl}$  and  $12\text{Mo}10\text{VAl}$ , possibly because of the detachment and recrystallization of dispersed  $\text{VO}_x$  structures during subsequent impregnation with  $\text{MoO}_x$  precursors. As  $\text{MoO}_x$  surface densities exceed one equivalent  $\text{MoO}_x$  monolayer in  $20\text{Mo}10\text{VAl}$ , intense bands appear at 1000, 823, 680, and  $320\text{ cm}^{-1}$ , corresponding to crystalline  $\text{MoO}_3$ .

Figure 6 shows Raman spectra for  $12\text{CrAl}$  and  $x\text{V}12\text{CrAl}$  ( $x = 3-15$ ;  $2.1-9.5\text{ V/nm}^2$ ) samples, which contain an equivalent  $\text{CrO}_x$  monolayer ( $7.9\text{ Cr/nm}^2$ ).<sup>63</sup> Polychromates, with Raman bands at  $750-900\text{ cm}^{-1}$ , are the predominant structures for  $\text{CrO}_x$  species supported on pure  $\text{Al}_2\text{O}_3$ , especially at  $\text{CrO}_x$  surface densities above  $3\text{ Cr/nm}^2$ .<sup>55,56,64,65</sup> The  $12\text{CrAl}$  sample shows three intense bands at 1009, 879, and  $799\text{ cm}^{-1}$ . The  $1009\text{ cm}^{-1}$

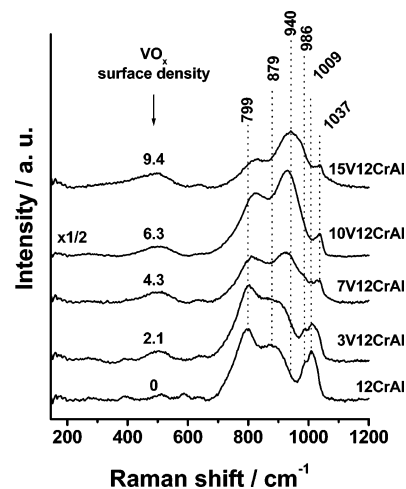


**Figure 6.** Raman spectra of  $12\text{CrAl}$  and  $x\text{V}12\text{CrAl}$  ( $x = 3-15$ ) treated in flowing dry air at 673 K for 1 h.

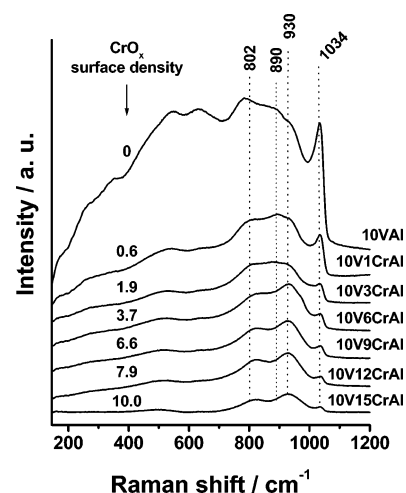


**Figure 7.** Raman spectra of  $10\text{VAl}$  and  $10\text{V}_x\text{CrAl}$  ( $x = 1-15$ ) treated in flowing dry air at 673 K for 1 h.

band arises from symmetric stretches in the  $\text{O}=\text{Cr}=\text{O}$  group within chromates, while the 879 and  $799\text{ cm}^{-1}$  bands reflect  $\text{Cr}-\text{O}-\text{Cr}$  stretches in dichromates and trichromates, respectively.<sup>56,64</sup> The weak band at  $986\text{ cm}^{-1}$  is assigned to  $\text{CrO}_3$  (bands at 975 and  $495\text{ cm}^{-1}$ ),<sup>56</sup> but crystalline  $\text{Cr}_2\text{O}_3$  (with a band at  $550\text{ cm}^{-1}$ ) was not detected in any of the samples.<sup>39, 56</sup>

Raman bands at 1009, 986, 879, and  $799\text{ cm}^{-1}$  weakened upon addition of  $\text{VO}_x$  to  $12\text{CrAl}$  samples and were ultimately replaced by a band at  $1037\text{ cm}^{-1}$  assigned to  $\text{V}=\text{O}$  stretches and by two broad bands at 940 and  $820\text{ cm}^{-1}$ . The broad nature of these two latter bands suggests that they arise from well-dispersed structures. Definitive assignment of the band at  $940\text{ cm}^{-1}$  is not possible. It appears at a frequency similar to that for orthorhombic  $\text{CrVO}_4$  ( $924\text{ cm}^{-1}$ ),<sup>66,67</sup> but the absence of corresponding diffraction lines suggests that it exists as disordered and highly dispersed  $\text{CrVO}_4$  domains, which tend to form at low temperature.<sup>68-70</sup> The origin of the  $830\text{ cm}^{-1}$  band is unclear; it may reflect the presence of polychromates, polyanadates, or mixed  $\text{V}-\text{O}-\text{Cr}$  oligomers. Crystalline  $\text{V}_2\text{O}_5$  was not detected, even at the highest  $\text{VO}_x$  surface density ( $15\text{V}12\text{CrAl}$ ;  $9.4\text{ V/nm}^2$ ).

Figure 7 shows Raman spectra for  $10\text{VAl}$  and  $10\text{V}_x\text{CrAl}$  ( $x = 1-15$ ) samples with an equivalent  $\text{VO}_x$  monolayer dispersed on  $\text{CrAl}$  supports at varying  $\text{CrO}_x$  surface densities. The relative intensities of bands at  $700-1000\text{ cm}^{-1}$  change with increasing  $\text{Cr}$  content. Bands at 786 and  $890\text{ cm}^{-1}$  in  $10\text{VAl}$  became

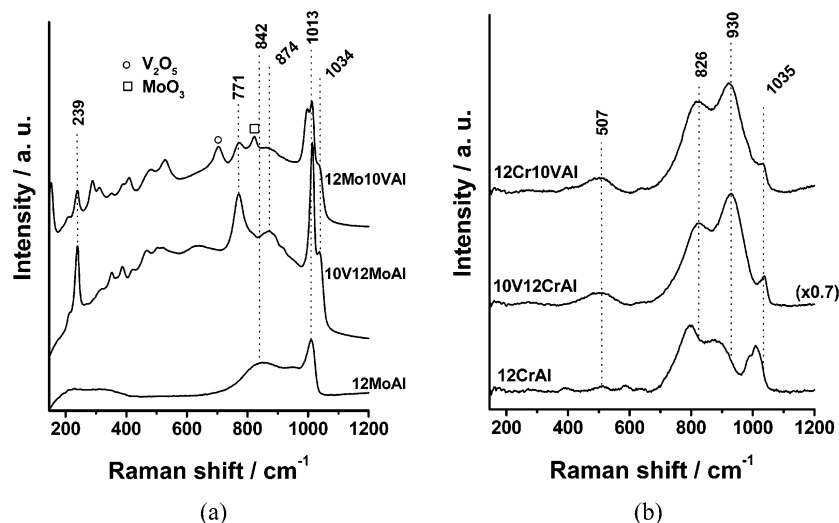


**Figure 8.** Raman spectra of (a) 12MoAl, 10V12MoAl, and 12Mo10VAI and (b) 12CrAl, 10V12CrAl, and 12Cr10VAI.

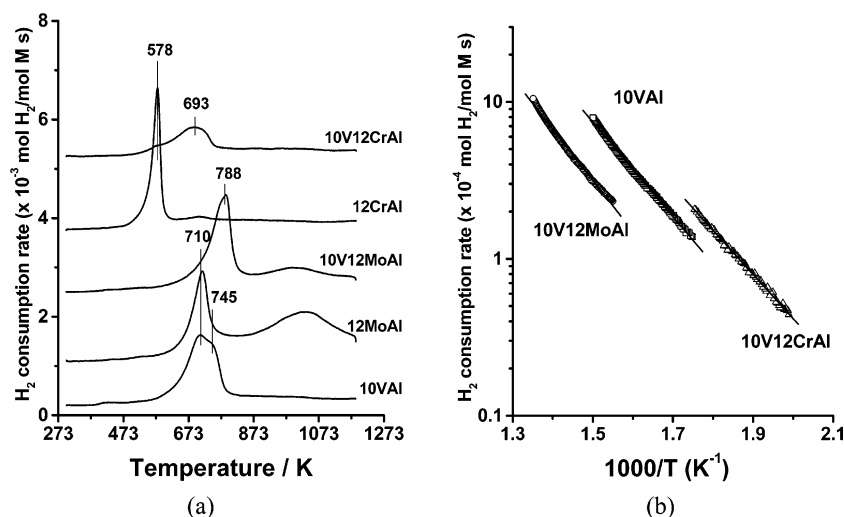


**Figure 9.** (a) TPR profiles of 10VAI, 12MoAl, 10V12MoAl, 12CrAl, and 10V12CrAl catalysts and (b) Arrhenius plots of the initial rate of H<sub>2</sub> consumption during TPR.

weaker, while the 930 cm<sup>-1</sup> band became stronger, possibly due to CrVO<sub>4</sub> formation. Only the 820 and 930 cm<sup>-1</sup> bands remained at CrO<sub>x</sub> surface densities above 3.7 Cr/nm<sup>2</sup>. The replacement of multiple bands for polyvanadates in 10VAI (Figure 2) with two bands at 820 and 930 cm<sup>-1</sup> in xV12CrAl ( $x = 7-15$ ) suggests that VO<sub>x</sub> species formed CrVO<sub>4</sub> species or dispersed more uniformly on CrO<sub>x</sub>-Al<sub>2</sub>O<sub>3</sub> than on pure Al<sub>2</sub>O<sub>3</sub> supports.

Raman spectra for 12MoAl, 10V12MoAl, and 12Mo10VAI and those for 12CrAl, 10V12CrAl, and 12Cr10VAI are compared in Figure 8a and b. Mixed Mo-O-V structures were detected on both 10V12MoAl and 12Mo10VAI. The spectra for 10V12CrAl and 12Cr10VAI are very similar, suggesting that the binary dispersed oxide structures formed are essentially independent of deposition sequence. Both spectra show a band at 930 cm<sup>-1</sup>, similar to that observed in CrVO<sub>4</sub> (924 cm<sup>-1</sup>).<sup>66,67</sup>

**3.1.2. Reduction of the Catalysts.** Figure 9a shows reduction profiles for 10VAI, 12MoAl, 10V12MoAl, 12CrAl, and 10V12CrAl. The 10VAI sample shows a peak at 710 K with a shoulder at 745 K, previously assigned to reduction of V<sup>5+</sup> to V<sup>3+</sup> in various polyvanadates,<sup>23,50</sup> and consistent with multiple Raman bands at 700–1000 cm<sup>-1</sup> in 10VAI (Figure 2). The 12MoAl sample shows a peak at 716 K, attributed to Mo<sup>6+</sup> reduction to Mo<sup>4+</sup> in dispersed MoO<sub>x</sub>, and another peak at 1033 K, corresponding to Mo<sup>4+</sup> reduction to Mo<sup>0</sup>.<sup>23,50,71</sup> The H<sub>2</sub>/Mo

ratios for the reduction peaks at 716 and 1033 K are 0.86 and 2.02, respectively, consistent with their respective assignments.

The reduction profile for 10V12MoAl also shows two peaks; the first peak (788 K) is attributed to the simultaneous reduction of Mo<sup>6+</sup> and V<sup>5+</sup> in V-Mo-O structures to Mo<sup>4+</sup> and V<sup>3+</sup>, respectively, while the peak at 1000 K reflects the reduction of Mo<sup>4+</sup> to Mo<sup>0</sup>. The reduction profiles for 10V12MoAl and 12Mo10VAI are very similar (Figure 10a) except for a slightly lower temperature for the first reduction peak in 12Mo10VAI (760 vs 786 K). Table 4 lists the assignments of each reduction peak and the moles of H<sub>2</sub> consumed per mole of metal. This table also shows the expected (stoichiometric) consumption of H<sub>2</sub> in each case. Measured H<sub>2</sub> consumption ratios are very similar to those expected for each reduction peak and for the total extent of reduction in 12MoAl, 10VAI, 10V12MoAl, and 12Mo10VAI samples.

Reduction profiles for 12CrAl and 10V12CrAl are shown in Figure 9a; their interpretation is more complex than from Mo-V systems, because of the tendency of CrO<sub>x</sub> structures to autoreduce to various extents during thermal treatments. The peak at 578 K for 12CrAl corresponds to reduction of Cr<sup>6+</sup> to Cr<sup>3+</sup>.<sup>39,40</sup> Table 4 shows, however, that measured H<sub>2</sub> consumptions for reduction of CrO<sub>x</sub> species are smaller than expected for the reduction of all Cr atoms in the sample from Cr<sup>6+</sup> to Cr<sup>3+</sup>, suggesting that only ~60% of Cr cations exist as Cr<sup>6+</sup> in 12CrAl

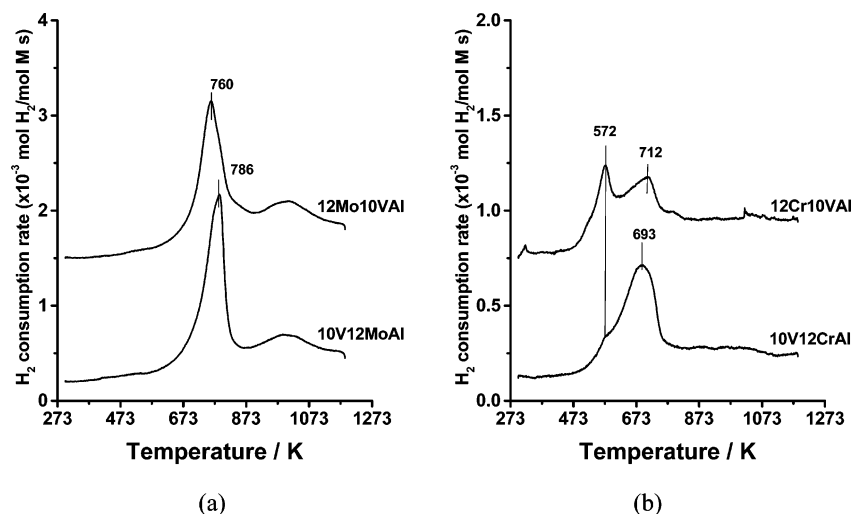


Figure 10. Comparison of TPR profiles for (a) 10V12MoAl and 12Mo10VAI and (b) 10V12CrAl and 12Cr10VAI.

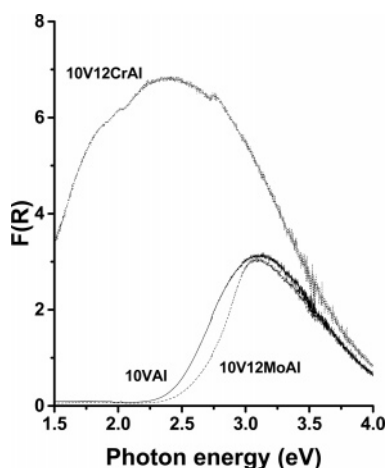


Figure 11. UV-visible spectra of 10VAI, 10V12MoAl, and 10V12CrAl treated at 723 K in flowing dry air for 0.5 h.

after thermal treatment in air. This proposal was confirmed by the fraction of the Cr as  $\text{Cr}^{6+}$  in  $x\text{CrAl}$  ( $x = 1-12$ ) (see Figure A of Supporting Information); in these samples, the fraction of the Cr as  $\text{Cr}^{6+}$  decreased monotonically from unity to 0.6 as  $x$  increased from 1 to 12 (i.e., 0.5–8  $\text{Cr}/\text{nm}^2$ ). Oxide supports stabilize surface chromate species in hexavalent form, but Cr atoms in excess of those required for a polychromate monolayer form a three-dimensional structure that reduces to trivalent species to form  $\text{Cr}_2\text{O}_3$  during thermal treatment in air.<sup>64,72–74</sup> Our findings indicate that such  $\text{Cr}^{3+}$  structures start to form at  $\text{CrO}_x$  surface densities above  $> 2 \text{ Cr}/\text{nm}^2$ .

TABLE 4: Assignments of TPR Results Reported in Figures 9 and 10

sample	reduction peak temperature (K)	assignment	$\text{H}_2/\text{M}$ (M = V, Mo, or Cr) (theoretical values are given in parentheses)
10VAI	710–745	$\text{V}^{5+} \rightarrow \text{V}^{3+}$	0.92 ( $\text{H}_2/\text{V} = 1$ )
12MoAl	710	$\text{Mo}^{6+} \rightarrow \text{Mo}^{4+}$	0.86 ( $\text{H}_2/\text{Mo} = 1$ )
	1053	$\text{Mo}^{4+} \rightarrow \text{Mo}^0$	2.02 ( $\text{H}_2/\text{Mo} = 2$ )
12CrAl	578	$\text{Cr}^{6+} \rightarrow \text{Cr}^{3+}$	0.91 ( $\text{H}_2/\text{Cr} = 1.5$ )
10V12MoAl	786	$\text{V}^{5+} \rightarrow \text{V}^{3+}$	0.99 ( $\text{H}_2/(\text{V} + \text{Mo}) = 1$ )
		$\text{Mo}^{6+} \rightarrow \text{Mo}^{4+}$	
	1053	$\text{Mo}^{4+} \rightarrow \text{Mo}^0$	1.9 ( $\text{H}_2/\text{Mo} = 2$ )
12Mo10VAI	760	$\text{V}^{5+} \rightarrow \text{V}^{3+}$	0.89 ( $\text{H}_2/(\text{V} + \text{Mo}) = 1$ )
		$\text{Mo}^{6+} \rightarrow \text{Mo}^{4+}$	
	1053	$\text{Mo}^{4+} \rightarrow \text{Mo}^0$	2.1 ( $\text{H}_2/\text{Mo} = 2$ )
10V12CrAl	572	$\text{Cr}^{6+} \rightarrow \text{Cr}^{3+}$	0.12 ( $\text{H}_2/\text{Cr} = 1.5$ )
	693	$\text{V}^{5+} \rightarrow \text{V}^{3+}$	1.08 ( $\text{H}_2/\text{V} = 1$ )
12Cr10VAI	572	$\text{Cr}^{6+} \rightarrow \text{Cr}^{3+}$	0.29 ( $\text{H}_2/\text{Cr} = 1.5$ )
	712	$\text{V}^{5+} \rightarrow \text{V}^{3+}$	0.91 ( $\text{H}_2/\text{V} = 1$ )

The 10V12CrAl samples show two overlapping reduction features at 578 and 693 K, which were assigned to  $\text{CrO}_x$  and  $\text{VO}_x$  reduction, respectively. The  $\text{CrO}_x$  reduction peak in 10V12CrAl appears as a small shoulder next to the  $\text{VO}_x$  reduction peak, even though the number of lattice oxygens associated with  $\text{VO}_x$  and  $\text{CrO}_x$  in this sample are similar, indicating that the fraction of the Cr atoms as  $\text{Cr}^{6+}$  in 10V12CrAl is significantly smaller than that in 12CrAl. In contrast, all  $\text{V}^{5+}$  reduce to  $\text{V}^{3+}$  in this sample. These data indicate that the deposition of a nominal monolayer of  $\text{VO}_x$  on 12CrAl leads to the reaction of most  $\text{CrO}_x$  species with  $\text{VO}_x$  to form dispersed  $\text{CrVO}_4$  during thermal treatment.

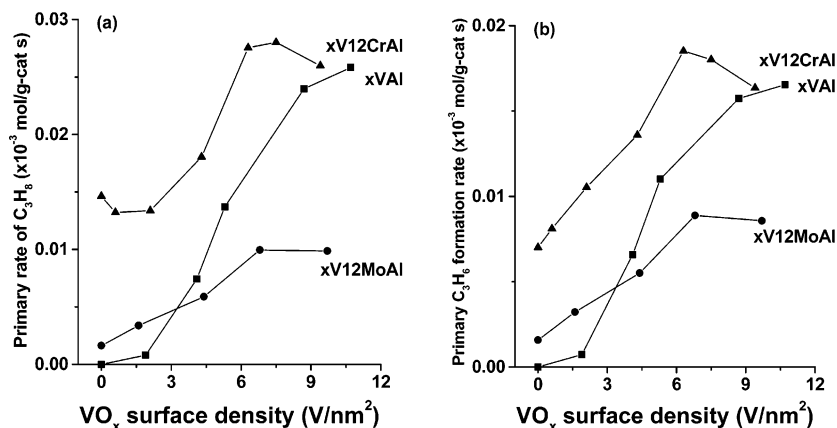
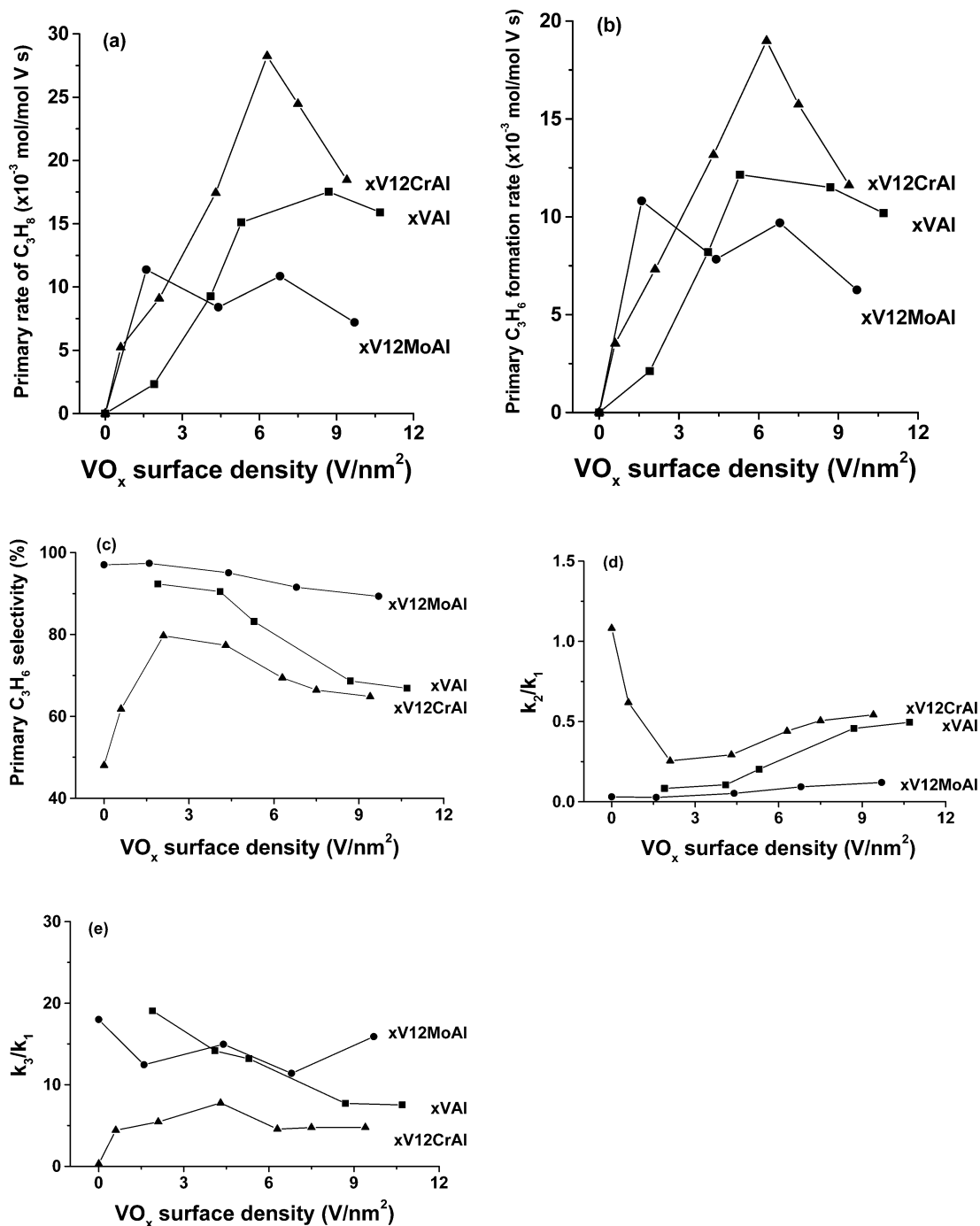


Figure 12. Weight-based activity of  $x\text{VAI}$ ,  $x\text{V12MoAl}$ , and  $x\text{V12CrAl}$  for (a)  $\text{C}_3\text{H}_8$  consumption and (b)  $\text{C}_3\text{H}_6$  formation.



**Figure 13.** Effect of VO<sub>x</sub> surface density on the reactivity of VAl, VmoAl, and VCrAl at 673 K: (a) primary rate of propane consumption; (b) primary rate of propene formation; (c) primary selectivity to propene; (d)  $k_2/k_1$  and (e)  $k_3/k_1$ . Reaction conditions:  $P_{C_3H_8} = 13.5$  kPa,  $P_{O_2} = 1.7$  kPa.

Reduction profiles for 12Cr10VAl and 10V12CrAl (Figure 10b) show that the CrO<sub>x</sub> reduction peak at 572 K is smaller in the latter sample. Consistent with this, Table 4 shows that the fraction of the Cr atoms present as Cr<sup>6+</sup> is higher in 12Cr10VAl than in 10V12CrAl; this indicates that 12Cr10VAl contains a smaller fraction of the CrO<sub>x</sub> as CrVO<sub>4</sub> than 10V12CrAl. This may be the reason that the reactivity of 12Cr10VAl is more similar to 12CrAl rather than 10VAl, as we report in the next section. The reduction profiles in Figure 9a indicate that VO<sub>x</sub> species reduce faster in 10V12CrAl than in 10VAl, while the MoO<sub>x</sub> layer in 10V12MoAl leads to slower VO<sub>x</sub> reduction than in 10VAl. Arrhenius plots of the initial H<sub>2</sub> consumption rates obtained during the early stages of the stoichiometric reduction of these oxides in H<sub>2</sub> (<15% reduction) are shown in Figure 9b. The initial H<sub>2</sub> consumption rates in 10V12CrAl are higher

than in 10VAl at all temperatures, while rates in 10V12MoAl are lower than in VAl. We expect and indeed find significant catalytic consequences of these reducibility trends for oxidative dehydrogenation reactions, as we discuss below.

**3.1.3. UV-Visible Characterization.** UV-visible spectra are shown in Figure 11 for 10VAl, 10V12MoAl, and 10V12CrAl. The spectra for 10VAl and 10V12MoAl are similar and show an absorption feature at 3.1 eV, while 10V12CrAl shows more intense absorption features, including two at 1.8 and 2.5 eV, corresponding to d-d transitions in Cr<sup>3+</sup> centers and charge transfer in polychromates,<sup>39,64</sup> without detectable spectral contributions from V<sup>5+</sup>.

UV-visible edge energies for 10VAl and 10V12MoAl samples are 2.25 and 2.40 eV, respectively. A previous study<sup>23</sup> reported that ODH turnover rates increased with decreasing

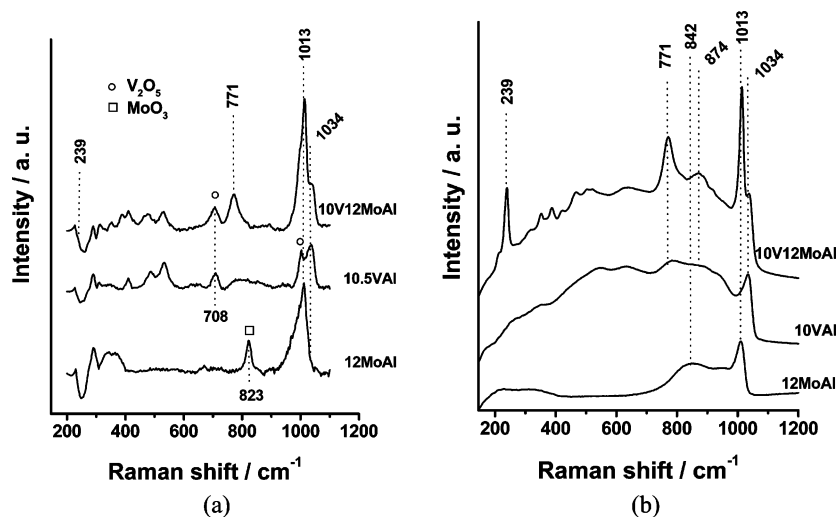


**Figure 14.** Comparison of Raman spectra for 12MoAl, 10VAl, and 10V12MoAl reported by Dai et al.<sup>50</sup> and those reported here.

absorption edge energy; thus, 10VAl would be expected to show lower ODH rates than 10V12MoAl, as found experimentally and reported below. The 10V12CrAl sample does not show an absorption edge, apparently because it occurs below 1.5 eV.

In summary, Raman, reduction, and UV–visible data indicate that polyvanadate structures predominate in VAl samples. Mixed metal oxides form when MoO<sub>x</sub> is placed below or above VO<sub>x</sub>, which leads to less reducible oxides and to higher absorption edge energies than in VAl. Raman and reduction results also show that most CrO<sub>x</sub> species react with VO<sub>x</sub> to form CrVO<sub>4</sub> when VO<sub>x</sub> is deposited over a nominal CrO<sub>x</sub> monolayer on Al<sub>2</sub>O<sub>3</sub>, but that some CrO<sub>x</sub> remains unreacted when it is deposited over a nominal monolayer of VO<sub>x</sub> on Al<sub>2</sub>O<sub>3</sub>.

### 3.2. Oxidative Dehydrogenation Rates and Selectivities.

Rates normalized by catalyst mass are shown in Figure 12 for C<sub>3</sub>H<sub>8</sub> conversion and C<sub>3</sub>H<sub>6</sub> formation on *x*VAl, *x*V12MoAl, and *x*V12CrAl as a function of VO<sub>x</sub> surface density. As reported previously,<sup>22</sup> ODH rates on *x*VAl increase with increasing VO<sub>x</sub> surface density and reach constant values at ~7 V/nm<sup>2</sup>. These trends reflect the higher VO<sub>x</sub> content and specific reactivity with increasing surface density, as more reactive polyvanadates replace less active and reducible monovanadate structures.<sup>23</sup>

VO<sub>x</sub> surface density effects on primary ODH rates (per V-atom) and selectivities and on rate constant ratios are shown in Figure 13 for *x*VAl, *x*V12MoAl, and *x*V12CrAl. For *x*V12MoAl and *x*V12CrAl, catalytic contributions from the part of the surface not covered by VO<sub>x</sub> species were subtracted from measured rates and residual VO<sub>x</sub> contributions were normalized by the V-atoms in each sample. This procedure assumes that the fraction of the support covered by VO<sub>x</sub> is proportional to VO<sub>x</sub> surface density up to 7 V/nm<sup>2</sup> and that exposed Mo- and Cr-coated surfaces catalyze reactions with rates similar to those on 12MoAl and 12CrAl samples.

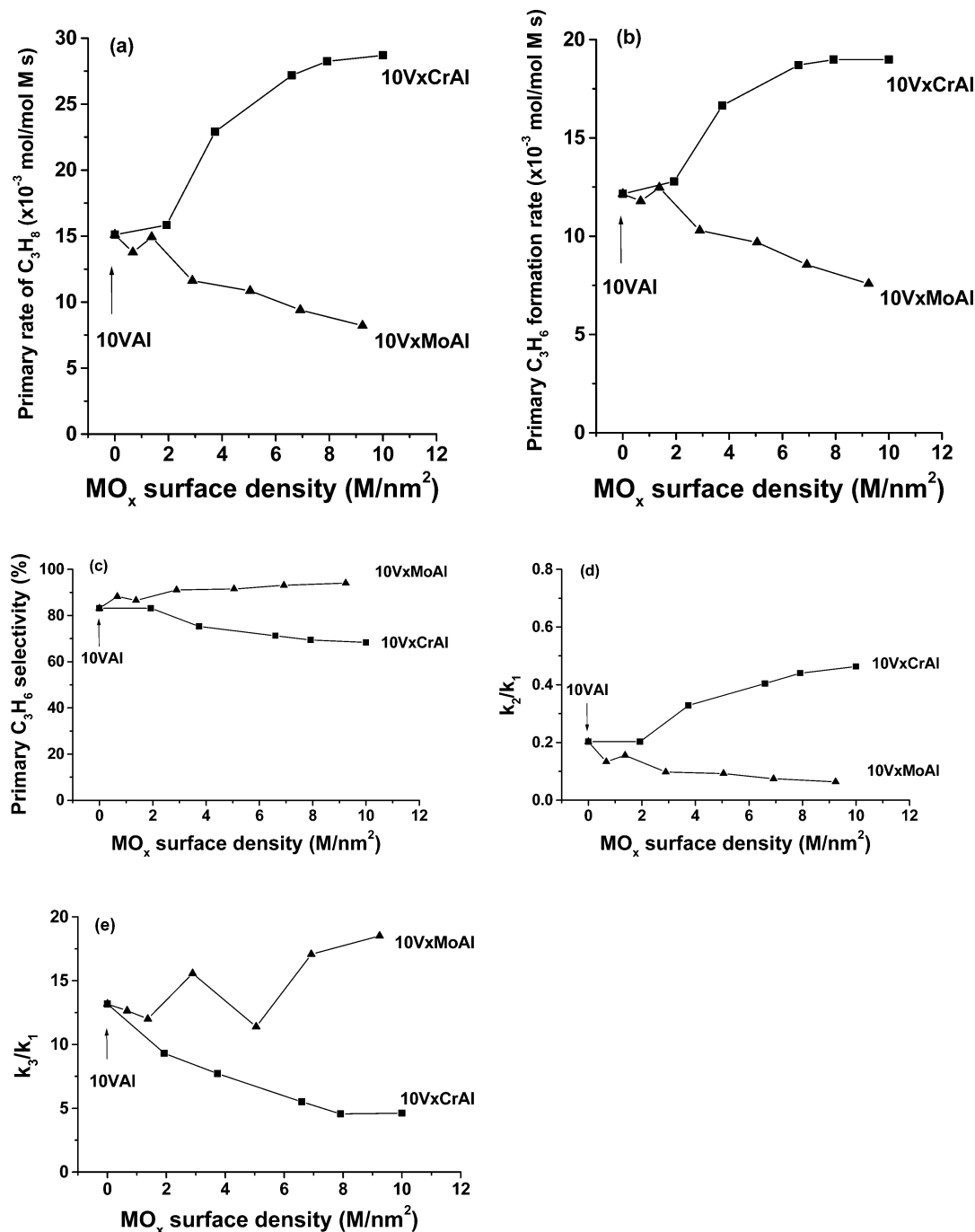
Primary rates for propane conversion and propene synthesis increased with increasing VO<sub>x</sub> surface density and reached maximum values at ~7 V/nm<sup>2</sup> on *x*VAl (Figure 13a and b), corresponding to an equivalent polyvanadate monolayer, as reported previously.<sup>22</sup> This trend reflects the higher reactivity of oligomeric VO<sub>x</sub> species relative to VO<sub>x</sub> monomers as the VO<sub>x</sub> coverage increases and is consistent with a concurrent decrease in absorption-edge energies and an increase in the rate of stoichiometric VO<sub>x</sub> reduction with H<sub>2</sub>.

Figure 13d and e shows that  $k_2/k_1$  ratios increase and  $k_3/k_1$  ratios decrease with increasing VO<sub>x</sub> surface density on *x*VAl.

These trends reflect the increasing propensity for propane to undergo combustion as the surface of alumina is covered by vanadia, and the tendency for propene to react less readily with increasing vanadia coverage. The latter trend is a consequence of the reduction in exposed alumina surface, on which are present Brønsted acid sites. A decrease in the exposure of such sites to the gas phase lowers the ease of readsorption of the newly formed olefin.

Effects of VO<sub>x</sub> surface density on primary ODH rates (per V-atom) are also observed on *x*V12MoAl and *x*V12CrAl. At low VO<sub>x</sub> surface densities (<3 V/nm<sup>2</sup>), rates on *x*V12MoAl and *x*V12CrAl are similar and higher than on *x*VAl. At higher VO<sub>x</sub> surface densities, rates on *x*V12MoAl become lower than on *x*VAl. This behavior appears to reflect the mixing of V and Mo species, leading to the replacement of V–O–V structures with less reactive V–O–Mo structures. Below 3 V/nm<sup>2</sup>, monovanadates prevail on both Al<sub>2</sub>O<sub>3</sub> and 12MoAl surfaces (Figure 3) and V–O–Al species in *x*VAl are thus replaced, at least in part, by V–O–Mo, leading to greater reducibility and ODH reaction rates. Above 3 V/nm<sup>2</sup>, polyvanadates form on *x*VAl, while mixed oxides form on *x*V12MoAl, leading to a net replacement of more reactive V–O–V species with less reactive V–O–Mo structures. Thus, active catalytic structures in polyvanadates are rendered less active by dilution with Mo–oxo linkages. This interpretation is consistent with the lower reduction rates and higher reduction peak temperature in 10V12MoAl than on 10VAl for samples containing predominantly polyvanadate and oligomeric Mo–O–V structures (Figure 9).

These effects of mixed VO<sub>x</sub> and MoO<sub>x</sub> structures differ from those reported previously;<sup>50</sup> that study reported that 10V12MoAl shows higher ODH rates (per V-atom) than 10VAl. These differences reflect the use of different VO<sub>x</sub> precursors used to prepare 10VAl (ammonium metavanadate) and 10V12MoAl (vanadyl isopropoxide) in the previous study.<sup>50</sup> Figure 14 shows Raman spectra for 12MoAl, 10.5VAl, and 10V12MoAl reported previously<sup>50</sup> and for identical compositions prepared by the methods used here (see Experimental Section). The use of ammonium heptamolydate and ammonium metavanadate as precursors led to low MoO<sub>x</sub> and VO<sub>x</sub> dispersions on alumina, as evidenced by the appearance of bands for MoO<sub>3</sub> and V<sub>2</sub>O<sub>5</sub> in these samples.<sup>50</sup> The bands for oligomeric MoO<sub>x</sub> and VO<sub>x</sub> are also less intense than those observed in the samples prepared for the present study. On the other hand, the samples of 10V12MoAl prepared previously<sup>50</sup> exhibit a Raman spectrum



**Figure 15.** Effect of  $\text{MoO}_x$  and  $\text{CrO}_x$  surface density on the reactivity of  $\text{VMoAl}$  and  $\text{VCrAl}$  at 673 K: (a) primary rate of propane consumption; (b) primary rate of propene formation; (c) primary selectivity to propene; (d)  $k_2/k_1$  and (e)  $k_3/k_1$ . Reaction conditions:  $P_{\text{C}_3\text{H}_8} = 13.5$  kPa,  $P_{\text{O}_2} = 1.7$  kPa.

very similar to that reported here, with clear evidence for Mo–O–V structures (1013, 771, and 239  $\text{cm}^{-1}$  bands). Thus, the higher ODH rates (per V-atom) reported earlier for 10V12MoAl relative to 10VAl are due predominantly to differences in synthetic methods. The results and conclusions in the present study are consistent with those of Bañares and Khatib,<sup>51</sup> who found no synergistic effects in  $\text{VO}_x\text{–MoO}_x/\text{Al}_2\text{O}_3$  samples prepared by coimpregnation of V and Mo precursors.

Figure 13d shows that  $k_2/k_1$  values are much lower on  $x\text{V12MoAl}$  than on  $x\text{VAl}$ , especially for  $\text{VO}_x$  surface densities above 5  $\text{V}/\text{nm}^2$ . Values of  $k_3/k_1$  are lower on  $x\text{V12MoAl}$  than on  $x\text{VAl}$  for  $\text{VO}_x$  surface densities below 4  $\text{V}/\text{nm}^2$ , but these trends are reversed at higher  $\text{VO}_x$  surface densities. At low surface densities, these effects reflect the coverage of  $\text{MoO}_x$

species by more selective  $\text{VO}_x$  domains, as shown by the higher value of  $k_3/k_1$  measured for a  $\text{MoO}_x$  monolayer on  $\text{Al}_2\text{O}_3$  than for a similar  $\text{VO}_x$  monolayer (Figure 13e). Thus, partial coverage of 12MoAl surfaces by  $\text{VO}_x$  would lead to the observed initial decrease in  $k_3/k_1$  values with increasing surface density in  $x\text{V12MoAl}$  samples. These effects are ultimately reversed as mixing of the  $\text{VO}_x$  and  $\text{MoO}_x$  structures occurs with increasing  $\text{VO}_x$  surface density, a process that leads to higher  $k_3/k_1$  ratios.

Primary ODH rates (per V-atom) on  $x\text{V12CrAl}$  exceed those on  $x\text{VAl}$ , even after subtracting contributions from exposed 12CrAl surfaces, at all  $\text{VO}_x$  surface densities (Figure 13). Both Raman spectra and reduction profiles for  $x\text{V12CrAl}$  indicate that  $\text{VO}_x$  increases the fraction of  $\text{CrO}_x$  that forms  $\text{CrVO}_4$ .

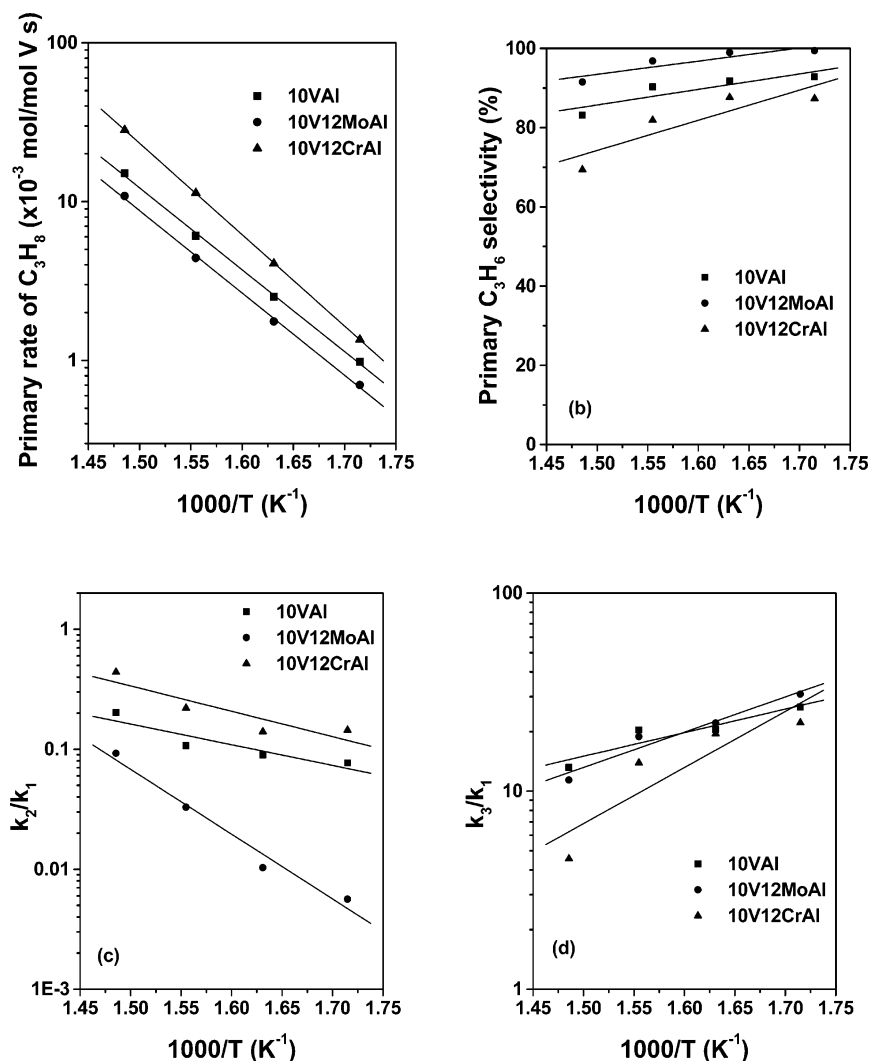


**Figure 16.** Comparison of the effects of temperature on the reactivity of 10VAl, 10V12MoAl, and 10V12CrAl: (a) primary rate of propane consumption; (b) primary selectivity to propene; (c)  $k_2/k_1$  and (d)  $k_3/k_1$ . Reaction conditions:  $P_{C_3H_8} = 13.5$  kPa,  $P_{O_2} = 1.7$  kPa.

Therefore, the higher specific ODH rates per V-atom of  $x$ V12CrAl relative to  $x$ VAl are attributed to the formation of V–O–Cr structures, which replace V–O–Al sites at low VO<sub>x</sub> surface densities. The value of  $k_2/k_1$  on 12CrAl (1.1) is higher than on 10VAl (0.2) and decreases with increasing VO<sub>x</sub> surface density up to 3 V/nm<sup>2</sup> (Figure 13d). Above this V-content,  $k_2/k_1$  increases with VO<sub>x</sub> surface density as in  $x$ VAl samples. Thus, the blocking of CrO<sub>x</sub> oligomers, with high propane combustion reactivity, by VO<sub>x</sub> reduces their contribution to combustion pathways, presumably because an increasing fraction of exposed surfaces consist of VO<sub>x</sub> or VCrO<sub>x</sub> domains. In contrast, values of  $k_3/k_1$  are very low on 12CrAl, and VO<sub>x</sub> deposition leads to higher values at low VO<sub>x</sub> surface densities, but ultimately to a decrease similar to that observed on  $x$ VAl as VCrO<sub>x</sub> species form with increasing surface density.

The interpretations of the effects of MoO<sub>x</sub> and CrO<sub>x</sub> underlayers on the structure and catalytic properties of VO<sub>x</sub> domains presented above are consistent with the data in Figure 15 for samples in which an equivalent VO<sub>x</sub> monolayer is deposited onto an Al<sub>2</sub>O<sub>3</sub> surface partly or fully covered by MoO<sub>x</sub> or CrO<sub>x</sub>. Partial MoO<sub>x</sub> coverages decreased ODH rate (per V-atom) because Mo–O–V bonds are less reactive than the V–O–V bonds prevalent in 10VAl at these VO<sub>x</sub> surface densities. With increasing MoO<sub>x</sub> surface density,  $k_2/k_1$  decreases and  $k_3/k_1$  increases. This is consistent with the lower  $k_2/k_1$  values and higher  $k_3/k_1$  ratios on MoO<sub>x</sub> than VO<sub>x</sub> domains (Figure 13).

Partial coverage of Al<sub>2</sub>O<sub>3</sub> by CrO<sub>x</sub> leads to effects opposite to those observed for equivalent MoO<sub>x</sub> coverages. ODH rates (per V-atom) increased monotonically, while  $k_2/k_1$  increased and  $k_3/k_1$  decreased, with increasing CrO<sub>x</sub> surface density.

Temperature effects on propane consumption, propene selectivity, and  $k_2/k_1$  and  $k_3/k_1$  ratios are shown in Figure 16 for similar VO<sub>x</sub> monolayers in 10VAl, 10V12MoAl, and 10V12CrAl. At all temperatures, the rate of propane conversion is higher for VO<sub>x</sub> dispersed on 12CrAl than on Al<sub>2</sub>O<sub>3</sub>, while VO<sub>x</sub> deposited onto 12MoAl leads to lower rates than on Al<sub>2</sub>O<sub>3</sub>. Propene selectivities are highest on 10V12MoAl and lowest on 10V12CrAl, with 10VAl giving intermediate values. On all three catalysts, propane consumption rates increased and propene selectivities decreased with increasing temperature; the latter reflects the observed increase in  $k_2/k_1$  with temperature, which arises from slightly higher activation energy for combustion than for dehydrogenation of propane. In contrast,  $k_3/k_1$  decreases markedly with increasing temperature, as expected from the lower activation energies involved in cleaving allylic C–H groups in propene as compared to those required for activation of stronger methylene C–H bonds in propane.<sup>19</sup> Temperature effects on  $k_2/k_1$  are stronger on 10V12MoAl than on 10VAl or 10V12CrAl samples, but temperature effects on  $k_3/k_1$  are more marked on 10V12CrAl than on 10VAl or 10V12MoAl.

The extent of mixing between an equivalent VO<sub>x</sub> monolayer and supports coated with MoO<sub>x</sub> or CrO<sub>x</sub> monolayers was probed

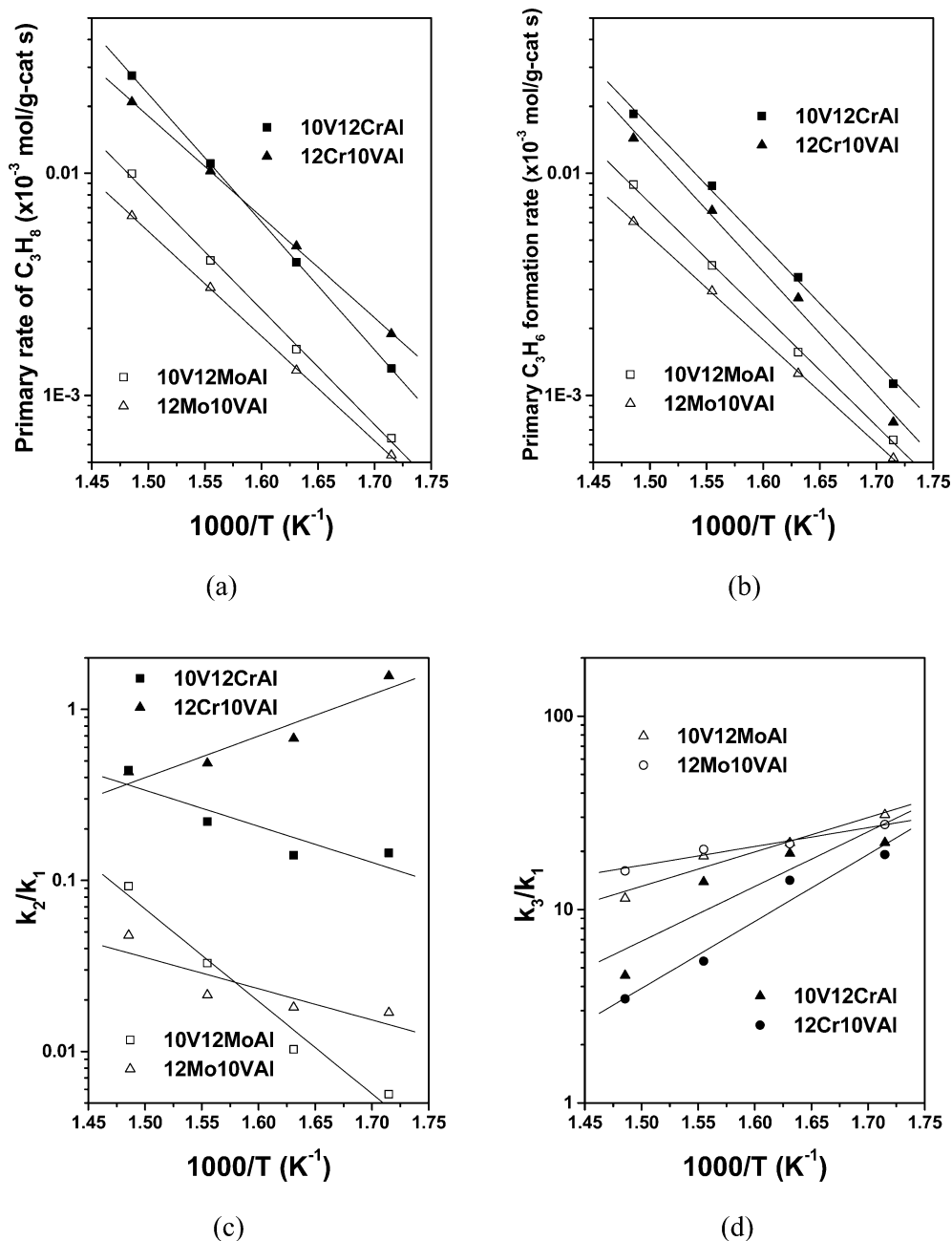


**Figure 17.** Comparison of the effects of temperature on the reactivity of 10V12MoAl, 12Mo10VAI, 10V12CrAl, and 12Cr10VAI: (a) primary rate of propane consumption; (b) primary selectivity to propene; (c)  $k_2/k_1$  and (d)  $k_3/k_1$ . Reaction conditions:  $P_{C_3H_8} = 13.5$  kPa,  $P_{O_2} = 1.7$  kPa.

by reversing the order of layer deposition. The effects of deposition sequence on dehydrogenation rates and on  $k_2/k_1$  and  $k_3/k_1$  ratios are shown as a function of temperature in Figure 17. Dehydrogenation rates (per mass) are 1.3 times higher at 673 K when MoO<sub>x</sub> was deposited first. Below 635 K,  $k_2/k_1$  is lower on 10V12MoAl than on 12Mo10VAI, but it becomes larger above 635 K, because of the stronger effects of temperature on  $k_2/k_1$  on the 10V12MoAl sample. Values of  $k_3/k_1$  are very similar on 10V12MoAl and 12Mo10VAI, although the value of  $k_3/k_1$  for 10V12MoAl decreases somewhat more rapidly with increasing temperature. These effects of deposition sequence reflect significant but incomplete mixing between VO<sub>x</sub> and MoO<sub>x</sub> monolayers. Raman spectra for 10V12MoAl and 12Mo10VAI showed bands for mixed Mo–O–V structures (Figure 8), especially when MoO<sub>x</sub> is deposited first (10V12MoAl), but their reduction profiles are very similar (Figure 10). These data, taken together with the observed catalytic consequences of deposition sequence (Figure 17), indicate that significant

mixing occurs during deposition or subsequent thermal treatment in VO<sub>x</sub>–MoO<sub>x</sub> binary dispersed oxide samples. The small remaining catalytic differences between 10V12MoAl and 12Mo10VAI reflect the presence of small amounts of VO<sub>x</sub> at 10V12MoAl surfaces and small amounts of MoO<sub>x</sub> at 12Mo10VAI surfaces.

For binary dispersed oxide samples containing equivalent monolayers of VO<sub>x</sub> and CrO<sub>x</sub>, the rate of propane ODH (per mass) is 1.5 times higher when CrO<sub>x</sub> is deposited first (10V12CrAl) instead of VO<sub>x</sub> (12Cr10VAI). The effects of temperature on  $k_2/k_1$  are strongly influenced by the sequence of deposition;  $k_2/k_1$  increases with temperature on 10V12CrAl, as was also found on 10VAI, but shows the opposite trend on 12Cr10VAI, as was also observed on 12CrAl. These effects of deposition sequence suggest that the surfaces of these dispersed binary oxides retain some of the properties of the oxide deposited last, even though most VO<sub>x</sub> and CrO<sub>x</sub> species interact to form mixed oxides, for example, CrVO<sub>4</sub>. Values of  $k_3/k_1$  are

higher on 10V12CrAl than on 12Cr10VAl and decrease with temperature on both samples. These data also suggest the predominant exposure of the oxide deposited last, because  $k_3/k_1$  values are lower on 12CrAl than on 10VAl (Figure 13), and both samples show a decrease in  $k_3/k_1$  ratios with increasing temperature (10VAl in Figure 16, temperature effects on 12CrAl not shown). These catalytic consequences of deposition order are much stronger than any structural changes detectable in their Raman spectra (Figure 8), from which it is not possible to assess the extent of mixing in 10V12CrAl and 12Cr10VAl. Reduction profiles for these two samples, however, provide definitive evidence for mixing of  $\text{VO}_x$  and  $\text{CrO}_x$  components in these samples. The reduction peak at 572 K (Figure 9), attributable to reduction of exposed  $\text{CrO}_x$  (Figure 8), is more pronounced in 12Cr10VAl than in 10V12CrAl, suggesting that  $\text{CrO}_x$  is preferentially exposed at the surface of 12Cr10VAl, consistent with the observed catalytic consequences of the deposition sequence.

#### 4. Conclusions

The deposition of vanadia on alumina covered by an equivalent monolayer of molybdena produces well-dispersed  $\text{VO}_x$  domains at low V surface densities and results in the formation of a mixed metal oxide ( $\text{AlMoVO}_4$ ) at higher V surface densities. This mixed metal oxide is less readily reducible than the polyvanadate species that form on the surface of alumina at an equivalent monolayer coverage. For V surface densities below 3  $\text{V}/\text{nm}^2$ , the specific activity of VMoAl catalysts for propane ODH is higher than that of VAl catalysts, but above this surface coverage the reverse relationship is observed. The ratio of the rate coefficients for propane combustion to ODH ( $k_2/k_1$ ) is significantly lower for VMoAl catalysts than for VAl catalysts, but the ratio of rate coefficients for propene combustion to propane ODH ( $k_3/k_1$ ) is more nearly comparable. No significant difference in structure or catalytic activity and selectivity was observed when the order of molybdena and vanadia deposition was reversed, suggesting that the two active oxides are intimately mixed. Deposition of vanadia on alumina covered by an equivalent monolayer of chromia produced well-dispersed  $\text{CrVO}_4$  species at all vanadia surface coverages. The reducibility of an equivalent monolayer of vanadia dispersed on the chromia-coated alumina is higher than that for an equivalent monolayer of vanadia on alumina. The propane ODH activity of such VCrAl catalysts is higher than that for VAl catalysts at all surface concentrations of vanadia. While the ratio of rate coefficients for propane combustion to ODH ( $k_2/k_1$ ) is larger for VCrAl catalysts than for VAl catalysts, the ratio of the rates coefficients for propene combustion to propane ODH ( $k_3/k_1$ ) is much lower for the former catalysts. For VCrAl catalysts, the order of deposition of the components affected the catalytic properties of the material formed. This suggests that some of the component last deposited on the surface remains not fully mixed with the component first deposited. The results of this study demonstrate the relationships between the structure and reactivity of binary dispersed oxides of vanadia and molybdena and of vanadia and chromia and illustrate strategies that can be used to prepare more active and selective alkane ODH catalysts.

**Acknowledgment.** This work was supported by the Director, Office of Basic Energy Sciences, Chemical Sciences Division of the U.S. Department of Energy under Contract DE-AC03-76SF00098.

**Supporting Information Available:** Figures of the percentage of Cr as  $\text{Cr}^{6+}$  in  $x\text{CrAl}$ ,  $x\text{V12CrAl}$ , and  $12\text{Cr10VAl}$

catalysts. This material is available free of charge via the Internet at <http://pubs.acs.org>.

#### References and Notes

- (1) Ross, J. R. H.; Smits, R. H. H.; Seshan, K. *Catal. Today* **1993**, *16*, 503.
- (2) Kung, H. H. *Adv. Catal.* **1994**, *40*, 1.
- (3) Mamedov, E. A.; Cortés-Corberan, V. *Appl. Catal., A* **1995**, *127*, 1.
- (4) Cavani, F.; Trifiro, F. *Catal. Today* **1995**, *24*, 307.
- (5) Centi, G.; Trifiro, F. *Appl. Catal., A* **1996**, *143*, 3.
- (6) Delmon, B.; Ruiz, P.; Carrazan, S. R. G.; Korili, S.; Rodriguez, M. A.; Vicente, Sobalik, Z. *Stud. Surf. Sci. Catal.* **1996**, *100*, 1.
- (7) Albonetti, S.; Cavani, F.; Trifiro, F. *Catal. Rev.-Sci. Eng.* **1996**, *38*, 413.
- (8) Vedrine, J. C.; Millet, J. M. M.; Volta, J.-C. *Catal. Today* **1996**, *32*, 115.
- (9) Blasko, T.; López Nieto, J. M. *Appl. Catal., A* **1997**, *157*, 117.
- (10) Kung, H. H.; Kung, M. C. *Appl. Catal., A* **1997**, *157*, 105.
- (11) Cavani, F.; Trifiro, F. *Catal. Today* **1999**, *51*, 561.
- (12) Grasselli, R. K. *Catal. Today* **1999**, *49*, 141.
- (13) Bhasin, M. M.; McCain, J. H.; Vora, B. V.; Imai, T.; Pujado, P. R. *Appl. Catal., A* **2001**, *221*, 397.
- (14) Sinev, M. Y. *J. Catal.* **2003**, *216*, 468.
- (15) Bhasin, M. M. *Top. Catal.* **2003**, *23*, 145.
- (16) Khodakov, A.; Yang, J.; Su, S.; Iglesia, E.; Bell, A. T. *J. Catal.* **1998**, *177*, 343.
- (17) Khodakov, A.; Olthof, B.; Bell, A. T.; Iglesia, E. *J. Catal.* **1999**, *181*, 205.
- (18) Chen, K.; Khodakov, A.; Yang, J.; Bell, A. T.; Iglesia, E. *J. Catal.* **1999**, *186*, 325.
- (19) Chen, K.; Bell, A. T.; Iglesia, E. *J. Phys. Chem. B* **2000**, *104*, 1292.
- (20) Olthof, B.; Khodakov, A.; Bell, A. T.; Iglesia, E. *J. Phys. Chem. B* **2000**, *104*, 1516.
- (21) Chen, K.; Iglesia, E.; Bell, A. T. *J. Catal.* **2000**, *192*, 197.
- (22) Argyle, M. D.; Chen, K.; Bell, A. T.; Iglesia, E. *J. Catal.* **2002**, *208*, 139.
- (23) Chen, K.; Bell, A. T.; Iglesia, E. *J. Catal.* **2002**, *209*, 35.
- (24) Garcia Cortez, G.; Fierro, J. L. G.; Banares, M. A. *Catal. Today* **2003**, *78*, 219.
- (25) Grabowski, R.; Sloczynski, J.; Grzesik, N. M. *Appl. Catal., A* **2003**, *242*, 297.
- (26) Christodoulakis, A.; Machli, M.; Lemonidou, A. A.; Boghosian, S. *J. Catal.* **2004**, *222*, 293.
- (27) Routray, K.; Reddy, K. R. S. K.; Deo, G. *Appl. Catal., A* **2004**, *265*, 103.
- (28) Ballarini, N.; Cavani, F.; Cericola, A.; Cortelli, C.; Ferrari, M.; Trifiro, F.; Capannelli, G.; Comite, A.; Catani, R.; Cornaro, U. *Catal. Today* **2004**, *91–92*, 99.
- (29) Grabowski, R. *Appl. Catal., A* **2004**, *270*, 37.
- (30) De, M.; Kunzru, D. *Catal. Lett.* **2004**, *96*, 33.
- (31) Pieck, C. L.; Banares, M. A.; Fierro, J. L. G. *J. Catal.* **2004**, *224*, 1.
- (32) Chen, K.; Xie, S.; Iglesia, E.; Bell, A. T. *J. Catal.* **2000**, *189*, 421.
- (33) Chen, K.; Xie, S.; Bell, A. T.; Iglesia, E. *J. Catal.* **2000**, *195*, 244.
- (34) Chen, K.; Iglesia, E.; Bell, A. T. *Stud. Surf. Sci. Catal.* **2001**, *136*, 507.
- (35) Chen, K.; Iglesia, E.; Bell, A. T. *J. Phys. Chem. B* **2001**, *105*, 646.
- (36) Chen, K.; Xie, S.; Bell, A. T.; Iglesia, E. *J. Catal.* **2001**, *198*, 232.
- (37) Abello, M. C.; Gomez, M. F.; Casella, M.; Ferretti, O. A.; Banares, M. A.; Fierro, J. L. G. *Appl. Catal., A* **2003**, *251*, 435.
- (38) Heracleous, E.; Lemonidou, A. A.; Lercher, J. A. *Appl. Catal., A* **2004**, *264*, 73.
- (39) Cherian, M.; Rao, M. S.; Hirt, A. M.; Wachs, I. E.; Deo, G. *J. Catal.* **2002**, *211*, 482.
- (40) Cherian, M.; Gupta, R.; Rao, M. S.; Deo, G. *Catal. Lett.* **2003**, *86*, 179.
- (41) Cherian, M.; Rao, M. S.; Deo, G. *Catal. Today* **2003**, *78*, 397.
- (42) Rao, T. V. M.; Deo, G.; Jehng, J.-M.; Wachs, I. E. *Langmuir* **2004**, *20*, 7159.
- (43) Jibril, B. Y.; Al-Zahrani, S. M.; Abasaheed, A. E.; Hughes, R. *Catal. Commun.* **2003**, *4*, 579.
- (44) Jibril, B. Y.; Al-Zahrani, S. M.; Abasaheed, A. E.; Hughes, R. *Catal. Lett.* **2003**, *3–4*, 121.
- (45) Al-Zahrani, S. M.; Jibril, B. Y.; Abasaheed, A. E. *Catal. Lett.* **2003**, *85*, 57.
- (46) Jibril, B. Y. *Appl. Catal., A* **2004**, *264*, 193.
- (47) Gilardoni, F.; Bell, A. T.; Chakraborty, A.; Boulet, P. *J. Phys. Chem. B* **2000**, *104*, 12250.
- (48) Gao, X. T.; Bare, S. R.; Fierro, J. L. G.; Wachs, I. E. *J. Phys. Chem. B* **1999**, *103*, 618.

- (49) Liu, H.; Cheung, P.; Iglesia, E. *Phys. Chem. Chem. Phys.* **2003**, *5*, 3795.
- (50) Dai, H.; Bell, A. T.; Iglesia, E. *J. Catal.* **2004**, *221*, 491.
- (51) Bañares, M. A.; Khatib, S. J. *Catal. Today* **2004**, *96*, 251.
- (52) Delgass, W. N. *Spectroscopy in Heterogeneous Catalysis*; Academic Press: New York, 1979.
- (53) Barton, D. G.; Shtein, M.; Wilson, R. D.; Soled, S. L.; Iglesia, E. *J. Phys. Chem. B* **1999**, *103*, 630.
- (54) Wachs, I. E. *Catal. Today* **1996**, *27*, 437.
- (55) Deo, G.; Wachs, I. E. *J. Phys. Chem.* **1991**, *95*, 5889.
- (56) Vuurman, M. A.; Wachs, I. E. *J. Phys. Chem.* **1992**, *96*, 5008.
- (57) Wachs, I. E.; Weckhuysen, B. M. *Appl. Catal., A* **1997**, *157*, 67.
- (58) Xie, S.; Iglesia, E.; Bell, A. T. *Langmuir* **2000**, *16*, 7162.
- (59) Chan, S. S.; Wachs, I. E.; Murrell, L. L. *J. Phys. Chem.* **1984**, *88*, 5831.
- (60) Hu, H.; Wachs, I. E.; Bare, S. R. *J. Phys. Chem.* **1995**, *99*, 10897.
- (61) Mestl, G.; Srinivasan, T. K. K. *Catal. Rev.-Sci. Eng.* **1998**, *40*, 451.
- (62) Xie, Y.-C.; Tang, Y.-Q. *Adv. Catal.* **1990**, *37*, 1.
- (63) Yang, G.; Haibo, Z.; Biying, Z. *J. Mater. Sci.* **2000**, *35*, 917.
- (64) Weckhuysen, B. W.; Wachs, I. E.; Schoonheydt, R. A. *Chem. Rev.* **1996**, *96*, 3327.
- (65) Vuurman, M. A.; Stufkens, D. J.; Oskam, A.; Moulijn, J. A.; Kapteijn, F. *J. Mol. Catal.* **1990**, *60*, 83.
- (66) Owen, O. S.; Kung, H. H. *J. Mol. Catal.* **1993**, *79*, 265.
- (67) Briand, L. E.; Jehng, J.-M.; Cornaglia, L.; Hirt, A. M.; Wachs, I. E. *Catal. Today* **2003**, *78*, 257.
- (68) Baran, E. J. *J. Mater. Sci.* **1998**, *33*, 2479.
- (69) Baudrin, E.; Denis, S.; Orsini, F.; Seguin, L.; Touboul, M.; Tarascon, J.-M. *J. Mater. Chem.* **1999**, *9*, 101.
- (70) Song, Z.; Matsushita, T.; Shishido, T.; Takehira, K. *J. Catal.* **2003**, *218*, 32.
- (71) Regalbutto, J. R.; Ha, J.-W. *Catal. Lett.* **1994**, *29*, 189.
- (72) Greenwood, N. N.; Earnshaw, A. *Chemistry of the Elements*; Pergamon Press: Elmsford, NY, 1989.
- (73) Hardcastle, F. D.; Wachs, I. E. *J. Mol. Catal.* **1988**, *46*, 173.
- (74) Vuurman, M. A.; Hardcastle, F. D.; Wachs, I. E. *J. Mol. Catal.* **1993**, *84*, 193.